A Novel Hybrid Finite Element-Spectral Boundary Integral Scheme for Modeling Earthquake Cycles: Application to Rate and State Faults with Low-Velocity Zones

Mohamed Abdelmeguid[1], Xiao Ma[1], Ahmed Elbanna[1]

[1]Department of Civil and Environmental Engineering, University of Illinois at Urbana-Champaign, Illinois, USA

Key Points:

- An efficient numerical scheme combining FEM-SBI for SEAS.
- LVFZ change the behavior of earthquake sequence and aseismic slip.
- Sub-surface events emerge for sufficiently compliant LVFZ and lead to slip deficit.
- Alternating event pattern is non montonically related to LVFZ width.

Corresponding author: Mohamed Abdelmeguid, `meguid@illinois.edu`

Abstract

We present a novel hybrid finite element (FE) - spectral boundary integral (SBI) scheme that enables efficient simulation of the slip evolution on faults, with near-field heterogeneities or nonlinearities, subjected to slow tectonic loading processes with episodes of spontaneously occurring events. This combined FE-SBI approach captures the benefits of finite elements in modelling problems with nonlinearities, as well as the computational superiority of SBI. The domain truncation enabled by this scheme allows us to utilize high-resolution finite elements discretization to capture inhomogeneities or complexities that may exist in a narrow region surrounding the fault. Combined with an adaptive time stepping algorithm, this framework opens new opportunities for modeling earthquake cycles with high-resolution fault zone physics. In this initial study, we consider a two dimensional (2-D) anti-plane model with a vertical strike-slip fault governed by rate and state friction. The proposed approach is first verified using the benchmark problem BP-1 from the SCEC SEAS repository. The computational framework is then utilized to model the earthquake sequence and aseismic slip of a fault embedded within a low-velocity fault zone (LVFZ) with different widths and compliance levels. Our results indicate that sufficiently compliant LVFZs contribute to the emergence of sub-surface events that fail to penetrate to the free surface and may experience earthquake clusters with nonuniform inter-seismic time. Furthermore, the LVFZ leads to slip rate amplification relative to the homogeneous elastic case. We discuss the implications of our results for understanding earthquake complexity as an interplay of fault friction and bulk heterogeneities.

1 Introduction

Earthquakes are among the costliest natural hazards on earth (D'Amico, 2016). The instabilities responsible for the onset and ensuing propagation of these events are linked to the fundamental physics of the heterogeneous and nonlinear topologically complex fault zones subjected to extreme geophysical conditions. Over sequences of seismic and aseismic slip, fault zones evolve continuously due to the feedback between nonlinear rheology, complex fault surface geometry, and both long range static and dynamic stress transfer. As there is insufficient data in the seismic catalog in the limit of large events (Lay, 2012), there is a strong need for developing computational tools that can accurately model the spatio-temporal patterns of earthquake ruptures and aseismic creep over long time scales and geologically relevant spatial scales to enable better understanding of these rare and large events, as well as to aid in policy making for hazard mitigation. However, this is far from being a trivial task due to the nonlinear and multi-scale nature of the problem.

The nonlinearity arises form a multitude of sources. Natural faults are usually embedded in a heterogeneous bed of rocks with variable elastic properties to begin with (Lewis & Ben-Zion, 2010; Yang et al., 2011) and a potential for yielding and fracture at different thresholds (Lyakhovsky et al., 2016). Furthermore, in most cases, the fault friction depends on the slip, slip rate, and deformations time history (Dieterich, 1979). The complex nature of this boundary condition makes an analytical solution only possible for a very limited number of model problems and necessitates solving the fracture problem numerically to predict the nucleation, propagation, and arrest conditions of the frictional instability (Nishioka & Atluri, 1982). The transitions in nonlinear rheology on fault surfaces, between rate weakening and rate strengthening, have been shown to contribute to the coseisemic and inter-seismic slip evolution on the fault surface (Rice, 1993; Noda & Lapusta, 2013). However, off-fault properties and bulk heterogeneities may also play a significant role in altering the earthquake cycle pattern (Erickson & Day, 2016). For example, ruptures that would load the bulk beyond its elastic limit, leading to the development of in-elasticity or damage around the fault, may lock in nonuniform stresses on the fault surface that would impact subsequent ruptures (Erickson et al., 2017).

Another significant challenge in the modeling of sequences of seismic and aseismic slip in fault zones is bridging the scales, both spatially and temporally. Spatially, an earthquake may involve several kilometers of fault rupture, whereas the principal slip surfaces, where most of the displacement is accommodated, may be in the order of a few millimeters (Rice, 2006). Between the two length scales, several topological features, including branches, distributed damage, and heterogeneous host rock, may exist (Chester et al., 1993). Temporally, to simulate a spontaneous earthquake sequence, the modeling approach should accommodate for slow tectonic loading during inter-seismic creep that could take years, rupture nucleation spanning over a few days, as well as the sudden release of energy associated with an earthquake rupture within seconds.

Earthquake cycle simulations, also referred to as sequences of earthquakes and aseismic slip (SEAS) models, aim to study the long term behavior of faults and lithospheric deformations on seismologically relevant spatio-temporal scales. They provide insight on the spontaneous nucleation and propagation of the seismic event, post-seismic response, and the aftershock sequences. For most naturally-occurring earthquakes, identifying initial conditions is almost impossible, thus a need arises for simulations that would provide unbiased insight regardless of the prescribed initial conditions. This is to be contrasted with simulations of a single seismic event in which the results depend critically on the prescribed initial stress and fault state. While in any SEAS simulation a portion of the earthquake sequence depends on the initial conditions of the system at the start of the simulation, the overall pattern would converge to a statistically steady solution independent of the initial conditions after this transitional stirring period. Various numerical approaches have been developed toward simplifying the modeling process of long term history of fault slip, mostly resorting to quasi-dynamic simulations that replace inertial dynamics during rupture propagation with a radiation damping approximation (Tse & Rice, 1986; Rice, 1993; Erickson & Dunham, 2014; Hillers et al., 2006; Y. Liu & Rice, 2007; Luo & Ampuero, 2018). Other numerical approaches involve switching between quasi-static approximation during slow deformation to a fully dynamic representation once instability nucleates (Okubo, 1989; Shibazaki & Matsu'ura, 1992). However, if this transition is done abruptly, it would introduce numerical artifacts that disrupt the development of the instability. Lapusta et al. introduced a rigorous procedure for simulating long term evolution of slip on planar faults in a homogeneous medium using a unified framework for both inertial dynamics and quasi-static inter-seismic deformation (Lapusta et al., 2004).

Attempts to model earthquake cycles falls under two main categories: domain-based approaches and boundary integral approaches. Domain-based methods are flexible in handling material nonlinearities and small-scale heterogeneities, as well as complexities of fault geometry (Kuna, 2013). However, modeling earthquake cycles with such methods is rare, partially because discretization of the entire domain is a computational bottleneck. To overcome one limitation of domain-based approaches that stems from the need to fully discretize a very large domain, a wide breadth of research has been directed toward finding appropriate truncation schemes that would shrink the simulated domain without affecting the physical solution, such as boundary viscous damping (Lysmer & Kuhlemeyer, 1969), infinite elements (Bettess, 1977), and perfectly matching layers (Berenger, 1994). While these approaches provide an adequate fix to the main problem, the computational cost would still be significant, as these absorbing boundaries need to be placed far away from the fault surface to avoid compromising the accuracy of the solution. Furthermore, many of these absorbing boundaries perform poorly in the quasi-static limit or if the incoming waves do not have normal incidence on the boundary.

Alternatively, boundary integral techniques limit the computations to the fault plane, effectively reducing the dimensions of the problem; thus, reducing the computational cost (Aliabadi, 2009). Lapusta et al. managed to integrate a spectral formulation of the boundary integral (SBI) method with a rigorous adaptive time-stepping scheme and introduced the concept of mode-dependent truncation in the evaluation of the time integration of the convolution integrals (Lapusta et al., 2004; Lapusta & Liu, 2009). Combining these features enabled long duration computations with slow tectonic loading marked by spontaneous occurrences of dynamic rupture in problems with planar faults in homogeneous media. However, this approach was only applicable to linear-elastic bulks. Furthermore, the lack of closed-form representation for the Green's function in the majority of situations meant that the ability of the method to provide well-defined solutions for domains with heterogeneities or fault roughness is compromised. The difficulty associated with finding a convenient spectral transformation of the space convolutions made computational investigation of problems with rough faults and fault zone complexity extremely convoluted and at times impossible using the SBI approach.

Hajarolasvadi and Elbanna introduced a framework that would consistently couple a domain-based approach (finite difference) and boundary integral scheme (spectral boundary integral) in what the authors referred to as a hybrid scheme (Hajarolasvadi & Elbanna, 2017). The proposed approach benefited from the strengths of each individual scheme without the drawbacks associated with it. In this framework, the region of complexity or nonlinearity is confined to a virtual strip that is discretized using finite difference. Through the consistent exchange of boundary conditions, the virtual strip was then coupled to two linearly elastic half-spaces, whereas the response of these half-spaces is captured by SBI. This framework proved to yield accurate results, at a fraction of the computational cost of a purely domain-based scheme. While initially developed to study the elastodynamics of an anti-plane problem, Ma et al. extended the hybrid method formulation to a 2-D in-plane setting and replaced the finite difference in the bulk with a finite element formulation (Ma et al., 2019), enabling more flexibility in handling complex boundaries and fault zone topologies (Ma & Elbanna, 2019).

In this paper, we extend the hybrid framework to model a sequence of earthquakes and aseismic slip. We focus our efforts in this initial study on examining the influence of elastic heterogeneity on the quasi-dynamic earthquake sequence that may emerge on a fault embedded in a low-velocity fault zone (LVFZ) undergoing slow tectonic loading. The LVFZ are damaged regions surrounding primary slip surfaces in which the seismic wave speed is lower than the that of the host rock, reflecting a more compliant structure. Low-velocity zones have been observed extensively, examples include San Andreas (Lewis & Ben-Zion, 2010; Y.-G. Li & Leary, 1990), Calico (Cochran et al., 2009), and North Anatolian (Ben-Zion et al., 2003) fault zones and thus understanding their implication for earthquake sequences is of special interest.

The remainder of the paper is organized as follows. In Section 2, we introduce the hybrid numerical scheme. We then verify the numerical implementation for the method using a benchmark problem from SCEC SEAS repository in Section 3.1. In Section 3.2, we summarize our results for the contribution of different realizations of low-velocity fault zones toward altering the sequence of earthquakes. We discuss the implications of our results and future extensions of this initial study in Section 4. Section 5 is reserved for concluding remarks.

2 Problem Formulation and Computational Framework

2.1 Governing Equations

We consider a domain Ω, with a prescribed traction boundary S_T, a displacement boundary S_u and one or more internal surfaces of discontinuities, or faults, along the boundary S_f. The equations of motion along with the appropriate boundary conditions are given by:

$$\begin{aligned} \rho\frac{\partial^2 u_i}{\partial t^2} - \frac{\partial \sigma_{ij}}{\partial x_j} - b_i &= 0 \quad in \quad \Omega \\ \sigma_{ij} n_j &= T_i \quad on \quad S_T \\ u_i &= u_i^0 \quad on \quad S_u \\ R_{ki}(u_i^+ - u_i^-) &= \delta_k \quad on \quad S_f \end{aligned} \tag{1}$$

where u_i is the displacement vector, and b_i is the body force vector. Slip is defined by $\delta_i = R_{ij}(u_j^+ - u_j^-)$, where R_{ij} is the rotation matrix that transforms the global coordinates to the local coordinate system of the fault and superscripts $+$ and $-$ indicate the plus and minus sides of the fault, respectively. If the fault plane is parallel to the x_1 axis, the slip simplifies to $\delta = u_1^+ - u_1^-$. σ_{ij} is the stress tensor. We assume body forces to be zero and the material behavior to be linear elastic:

$$\sigma_{ij} = \lambda\delta_{ij}\varepsilon_{kk} + 2\mu\varepsilon_{ij} \tag{2}$$

where ε_{ij} is the infinitesimal strain tensor, and μ, and λ are the Lamé parameters.

In this initial study, we restrict our implementation to the 2-D anti-plane shear deformation problem, in which the only nonzero component of the displacement is restricted to the x_3 direction. The body forces are assumed to be zero; accordingly, the balance of linear momentum reduces to:

$$\rho\frac{\partial^2 u_3}{\partial t^2} = \sigma_{13,1} + \sigma_{23,2} \tag{3}$$

where τ_{13} and τ_{23} are the shear components of stress. Considering only linearly elastic materials, the stress is given by:

$$\sigma_{13} = \mu \frac{\partial u_3}{\partial x_1} \tag{4}$$

$$\sigma_{23} = \mu \frac{\partial u_3}{\partial x_2} \tag{5}$$

where μ is the shear modulus which can have spatial dependencies. By substituting in the balance equation we obtain:

$$\rho \frac{\partial^2 u_3}{\partial t^2} = \frac{\partial}{\partial x_1}\left(\mu \frac{\partial u_3}{\partial x_1}\right) + \frac{\partial}{\partial x_2}\left(\mu \frac{\partial u_3}{\partial x_2}\right) \tag{6}$$

The slip constraint imposed on the governing equation then reduces to:

$$R_{k3}(u_3^+ - u_3^-) = \delta_k \quad on \quad S_f \tag{7}$$

Our main goal is to provide an efficient and accurate numerical scheme that is capable of solving this set of equations in an unbounded domain.

2.2 Hybrid Method Formulation

The hybrid formulation considered here is a combination of the finite element method (FEM) and the spectral boundary integral method (SBI) previously introduced by (Ma et al., 2019). The nonlinearities, such as fault surface roughness or material nonlinearity, as well as small-scale heterogeneities, are confined apriori in a virtual strip of a certain width. This virtual strip is then discretized and modeled using FEM. The rest of the domain, which is homogeneous and linear-elastic, is modeled using SBI as two half-spaces and coupled to the FEM domain on each side (S^+, S^-). The two methods enforce continuity by exchanging traction and displacement boundary conditions at those sides. The general setup of the hybrid method is shown in Figure 1. The width WH of the virtual strip depends on the nature of the problem and may be adjusted to contain the heterogeneities, nonlinearities, and other fault zone complexities.

2.2.1 Finite Element Method

The fault discontinuity implementation in the FEM is based on the domain decomposition approach outlined in (Aagaard et al., 2013). In this approach, the fault surface is considered to be an interior boundary between two domains with a + and − sides. The slip on the fault produces equal and opposite tractions on each of those sides, represented by a Lagrange multiplier. It follows that the weak form representation of this problem is give by:

$$-\int_V \sigma_{ij}\phi_{i,j} dV + \int_{S_T} T_i \phi_i dS - \int_V \rho \ddot{u}_i \phi_i dV - \int_{S_{f+}} T_i^{f^+} \phi_i dS + \int_{S_{f-}} T_i^{f^-} \phi_i dS = 0 \tag{8}$$

where ϕ is the weighting function. The integral along S_f accounts for the Lagrange multipliers (tractions) on the fault surfaces. $T_i^{f^+} = \sigma_{ij} n_j^+$ and $T_i^{f^-} = \sigma_{ij} n_j^-$ where n_j^+ and n_j^- are the fault normals for the positive and negative sides of the faults respectively. These boundary tractions are associated with the slip constraint on the fault shown in expression (7) and are imposed via Lagrange multipliers.

To account for the coupling between the FEM and SBI within the finite element formulation, we proceed as follows. We impose the tractions τ^{SBI} that accounts for the existence of the half-spaces as Neumann boundary conditions for the FEM strip. The value of τ^{SBI} is provided through the SBI formulation as will be discussed shortly. This ensures continuity of traction at the outer interfaces. Since the nodes along the outer interfaces share the same kinematic degrees of freedom between the virtual strip and the adjacent half-space, continuity of displacements is also automatically satisfied. Altogether, this leads to the following system of equations:

$$\begin{aligned} -\int_V \sigma_{ij}\phi_{i,j} dV + \int_{S^+_{SBI}} \tau_i^{+,SBI} \phi_i dS - \int_{S^-_{SBI}} \tau_i^{-,SBI} \phi_i dS - \int_V \rho \ddot{u}_i \phi_i dV \\ - \int_{S_{f+}} T_i^{f^+} \phi_i dS + \int_{S_{f-}} T_i^{f^-} \phi_i dS = 0 \end{aligned} \tag{9}$$

$$\int_{S_f} \phi_k \left[R_{ki}(u_i^+ - u_i^-) - d_k\right] = 0 \tag{10}$$

Here, we adopt a quasi-dynamic modeling framework where inertial effects are approximated with a radiation damping term when resolving shear tractions on the fault surface. Thus, time dependence enters through the constitutive models and the loading conditions only. While not capturing the full dynamic nature of the problem, this assumption is important since suppressing inertial terms entirely would result in an unbounded slip rate in finite time (Rice, 1993). The quasi-dynamic simulations reduce then to a series of static problems with potentially time-varying physical properties and boundary conditions. The temporal accuracy of the solution is limited to resolving these temporal variations. Considering deformations at time t and after suppressing the inertia term, the weak form may be written as:

$$\begin{aligned}-\int_V \sigma_{ij}(t)\phi_{i,j}dV + \int_{S^+_{SBI}} \tau_i^{+,SBI}(t)\phi_i dS - \int_{S^-_{SBI}} \tau_i^{-,SBI}(t)\phi_i dS \\ - \int_{S_{f+}} T_i^{f^+}(t)\phi_i dS + \int_{S_{f-}} T_i^{f^-}(t)\phi_i dS = 0\end{aligned} \tag{11}$$

$$\int_{S_f} \phi_k \left[R_{ki}(u_i^+(t) - u_i^-(t)) - d_k(t)\right] = 0 \tag{12}$$

with the understanding that fault tractions will be modified to account for radiation damping effects as we will describe shortly. Expressions (11) and (12) may be discretized using a Galerkin approach. Accordingly, we express the test function ϕ, trial solution u , Lagrange multipliers T^f, fault slip d, and SBI tractions τ^{SBI} as linear combinations of basis function:

$$\phi = \sum_m w_m N_m, \quad u = \sum_n u_n N_n, \quad T^f = \sum_p T_p^f N_p, \quad \tau^{SBI} = \sum_s \tau_s^{SBI} N_s, \quad d = \sum_p d_p N_p \tag{13}$$

where n is the number of functions associated with the domain displacements, p is the number of functions associated with fault surface, m is used to denote the number of basis functions for the test solutions, and s denotes the functions associated with the SBI degree of freedoms. Noting that the tractions on the fault are equal in magnitude, the weak form is transformed into:

$$\begin{aligned}-\int_V \nabla N_m^T \cdot \sigma(t) dV + \int_{S^+_{SBI}} N_m^T N_{s^+} \tau_{s^+}^{SBI}(t) dS - \int_{S^-_{SBI}} N_m^T N_{s^-} \tau_{s^-}^{SBI}(t) dS \\ - \int_{S_{f+}} N_m^T N_p T_p^f(t) dS + \int_{S_{f-}} N_m^T N_p T_p^f dS = 0\end{aligned} \tag{14}$$

$$\int_{S_f} N_p^T \left[R_{pn}(N_n u_n^+(t) - N_n u_n^-(t)) - N_p d_p(t)\right] = 0 \tag{15}$$

Assuming that the fault surface is aligned with the domain coordinate system these expressions are converted to a more compact matrix notation as:

$$\mathbf{K}u(t) + \mathbf{L}^T\left(\tau^{SBI}(t) + T^f(t)\right) = \mathbf{F}(t) \tag{16}$$

$$\mathbf{L}u(t) = \mathbf{D}(t) \tag{17}$$

This is a saddle point problem, in which it is important to choose the basis functions that would satisfy the Ladyženskaja-Babuška-Brezzi (LBB) stability condition (Urgen Bathe, 2001). For our problem, a choice of the same space of functions for the Lagrange multipliers and the displacement on the fault would ensure a stable system of equations.

2.2.2 Spectral Boundary Integral Method

The boundary integral method has been used extensively since the mid-1980s to study the propagation of cracks (Aliabadi, 2009). The main advantage of this method is that it eliminates the need to study wave propagation in the entire domain by using integral relationships between the displacement discontinuities and tractions along the crack path (Day et al., 2005).

The spectral formulation of this method gives an exact form of such a relationship in the Fourier domain. We use the spectral formulation introduced in (P. Geubelle & Rice, 1995), where the elastodynamic analysis of each half-space is carried out separately. In view of the hybrid method, where SBI constitutes a boundary condition to the FEM model through tractions τ^{SBI}, we focus the description on modeling a half-space. For brevity, we restrict our discussion to the anti-plane formulation of the SBI scheme. However, we note that the formulation of the independent SBI for a three-dimensional (3-D) domain may be readily incorporated in the hybrid scheme (Breitenfeld & Geubelle, 1998). The relationship between the traction τ_3 and the resulting displacements at the boundary of a half-space may be expressed as:

$$\tau_3^{\pm}(x_1,t) = \tau_3^{0\pm}(x_1,t) \mp \frac{\mu}{c_s}\dot{u}_3^{\pm}(x_1,t) \pm f_3^{\pm}(x_1,t) \tag{18}$$

where, $\tau_3^0(x_1,t)$ is the shear stress that would be present if the fault is locked, c_s is the shear wave speed, and $f_3^{\pm}(x_1,t)$ is a functional given by the space time convolution of the fundamental elastodynamic solution with prior history of slip along the fault line. This convolution term is expressed in the Fourier domain as:

$$f_3^{\pm}(x_1,t) = F_3^{\pm}(t;q)e^{iqx_1} \tag{19}$$

where q is the wave number. The Fourier coefficient $F_3^{\pm}(t;q)$ is given in terms of displacement Fourier coefficient $U_3(t;q)$ by the convolution integral (P. H. Geubelle & Breitenfeld, 1997):

$$F_3^{\pm}(t;q) = \mp\mu|q|\int_0^t H_{33}(|q|c_s t')U_3^{\pm}(t-t';q)|q|c_s \mathrm{d}t' \tag{20}$$

The convolution kernel of this independent formulation was shown to be $H_{33}(T) = J1(T)/T$ with $J1(T)$ as the first kind Bessel function of order one. This is identical to the convolution kernel of the combined formulation for the anti-plane problem (Lapusta et al., 2004).

Integration by parts would yield an analogous "velocity" representation in terms of $\dot{U}_3(t;q)$ that distinguishes between the static and dynamic contributions.

$$F_3^{\pm}(t;q) = \mp\mu|q|U_3(t;q) \pm \mu|q|\int_0^t W_{33}(|q|c_s t')\dot{U}_3^{\pm}(t-t';q)|q|c_s \mathrm{d}t' \tag{21}$$

The SBI may then be readily adjusted for the quasi-dynamic framework by only considering the static contribution of the convolution term $f_3(x_1,t)$. In this case, the Fourier coefficient $F_3(t;q)$ is given by:

$$F_3^{\pm}(t;q) = \mp\mu|q|U_3(t;q) \tag{22}$$

2.2.3 Frictional Framework

Here, we adopt a rate and state frictional (RSF) formulation (Dieterich, 1979; Ruina, 1983). The boundary condition on the fault surface is enforced by equating the fault shear stress to its strength:

$$\tau = F(V,\theta) = f(V,\theta)\sigma_n \tag{23}$$

where the fault strength F is defined in terms of the normal stress σ_n and the friction coefficient f. In the RSF, the friction coefficient depends on the slip rate V and state θ as:

$$f(V,\theta) = f_o + a\ln\left(\frac{V}{V_o}\right) + b\ln\left(\frac{\theta V_o}{L}\right) \tag{24}$$

where L is the characteristic slip distance, f_o is the reference friction coefficient defined at a slip rate V_o. The state evolution is prescribed through the aging law (J.R.Rice & A.L.Ruina, 1983), which is commonly applied to earthquake cycle simulations (Lapusta et al., 2004; Erickson & Dunham, 2014; Herrendörfer et al., 2018; Y. Liu & Rice, 2007) and defined as:

$$\frac{d\theta}{dt} = 1 - \frac{V\theta}{L} \tag{25}$$

This results in a steady-state solution of the state variable $\theta_{ss} = \frac{L}{V}$. The corresponding steady-state friction coefficient is given by:

$$f_{ss} = f_o + (a - b) \ln \left(\frac{V}{V_o} \right) \tag{26}$$

Here, the parameter combination $a - b > 0$ describes a steady state rate-strengthening frictional response and $a - b < 0$ describes a steady state rate-weakening frictional response.

In expression (24), the fault frictional strength becomes ill-posed at $V = 0$. To avoid this, we follow a regularized version of the RSF presented in (Ben-Zion & Rice, 1996) that permits solution near $V = 0$:

$$f(V, \theta) = a \sinh^{-1} \left[\frac{V}{2V_o} \exp \left(\frac{f_o + b \ln \left(\frac{\theta V_o}{L} \right)}{a} \right) \right] \tag{27}$$

Using an energy balance approach, Ampuero et al. established the following theoretical estimate for the nucleation size h^* of an anti-plane frictional crack under slow tectonic loading (Ampuero & Rubin, 2008):

$$h^* = \frac{2\mu L b}{\pi \sigma_n (b - a)^2} \tag{28}$$

This nucleation size defines the critical wavelength that has to be resolved within the numerical scheme and is valid for $a/b > 0.5$.

In addition to the nucleation size, Dieterich presented another characteristic length scale L_b, which is associated with the process zone during the propagation of the rupture when $V\theta/L >> 1$ and scales as b^{-1} (Dieterich, 1992). For anti-plane perturbations L_b is given as:

$$L_b = \frac{\mu L}{\sigma_n b} \tag{29}$$

It is vital to properly resolve this length scale as it is more stringent than the nucleation zone's length. In our computational framework we always ensure that h^* and L_b are both well resolved.

2.2.4 Time Stepping

To predict the response of the domain at $t+dt$, we solve the system of equations in expressions (16) and (17) starting from a known state at time t, including slip $d(t)$ and state variable $\theta(t)$, and subjected to a time-dependent boundary condition $u_b(t)$ on S_u and traction boundary conditions $\tau^{SBI}(t)$ on the virtual boundaries. The updating algorithm is then given as follows:

1. Use $u(t - \triangle t)$ as a predictor for $u(t)$ on S_{SBI}.

$$u^*_{SBI}(t) = u_{SBI}(t - \triangle t) \tag{30}$$

2. Make a corresponding prediction for the convolution functional $f^*(t)$ using the displacement assumption (30). This is done by computing the Fourier coefficients of $u^*(t)$ such that:

$$u^*_{SBI}(t) = \sum_{s=-n_s/2}^{n_s/2} U^*_s(t) e^{iq_s z}, \quad q_s = \frac{2\pi s}{\lambda} \tag{31}$$

   where λ is the length of the SBI domain under consideration, and n_s is the number of FFT sample points used to discretize the domain. Then, using expression (22), we compute the Fourier coefficients of the functional.

$$F^*_s(t; q) = \mp \mu |q_s| U^*_s(t; q) \tag{32}$$

   The functional is then recovered in the real space using inverse FFT as:

$$f^*(t) = \sum_{s=-n_s/2}^{n_s/2} F^*_s(t) e^{iq_s z} \tag{33}$$

3. Write $\tau^{SBI*}(t)$ assuming no initial tractions imposed on S_{SBI} as:

$$\tau^{SBI*,\pm}(t) = \mp\frac{\mu}{c_s}\dot{u}_{SBI}(t) + f^*(t) \tag{34}$$

   where $\dot{u}_{SBI}(t)$ is still an unknown quantity that depends on $u_{SBI}(t)$. Thus, we use a backward Euler approximation:

$$\dot{u}_{SBI}(t) = \frac{u_{SBI}(t) - u_{SBI}(t-\triangle t)}{\triangle t} \tag{35}$$

4. Find a new prediction for $u^{**}(t)$ by solving the elasticity equations in expressions (16) and (17) now rearranged as:

$$\mathbf{K}u^{**}(t) + \mathbf{L}^T\left(\mp\frac{\mu}{c_s\triangle t}u^{**}_{SBI}(t) + T^f(t)\right) = \mathbf{F}(t) - \mathbf{L}^T\left(\pm\frac{\mu}{c_s\triangle t}u_{SBI}(t-\triangle t) + f^*(t)\right) \tag{36}$$

$$\mathbf{L}u(t) = \mathbf{D}(t) \tag{37}$$

5. Correct $u_{SBI}(t)$ by using both predictions:

$$u_{SBI}(t) = \frac{1}{2}\left[u^*_{SBI}(t) + u^{**}_{SBI}(t)\right] \tag{38}$$

6. Repeat Steps 2-4 using the corrected $u_{SBI}(t)$ and obtain fault tractions T^f from the Lagrange multipliers.
7. Find the value of the slip rate $V(t)$ corresponding to fault tractions T^f. This is done in a quasi-dynamic framework by equating the fault tractions to the fault strength plus radiation damping component to get:

$$T^f = F(V,\theta) + \eta V \tag{39}$$

   where $\eta = \mu/2c_s$ is half the shear-wave impedance, μ is the shear modulus, and c_s is the shear wave speed of the elements adjacent to the fault. This is a nonlinear equation that we solve using a safe-gaurded Newton-Raphson scheme (quadratic convergence), with the safe-guard being an embedded Secant scheme (superlinear convergence).
8. Obtain state $\theta(t+\triangle t)$ and slip $d(t+\triangle t)$ using Runge-Kutta-Fehlberg (RKF45), a fourth order accurate scheme with a fifth order accurate error estimate. The RKF45 accounts for the adaptivity in time stepping.
9. Return to step 1 to proceed further in time.

To ensure accuracy, we restrict our time step to a fraction of L/V such that the slip increment in a time step is bounded to be smaller than the characteristic length scale in the rate and state friction law. Here, we choose this upper bound following (Lapusta et al., 2004) but other options will be further investigated in the future. We note that within the RKF45 algorithm, Steps 1-7 are evaluated at each increment within the time step .

Algorithm 1 outlines the entire proposed procedure in which we time march from a given start at time t to $t + \triangle t$.

Algorithm 1: Time Advance Algorithm

while $t < t_{final}$ **do**
  At time t, $d(t)$, $\theta(t)$, $u_b(t)$ and $u(t-\triangle t)$ are known;
  1. Using $u^*(t)$ estimate $\tau_s^{SBI*}(t)$;
  2. Solve the linear equations (36) and (37) for $u^{**}(t)$;
  3. Obtain a correction for $\tau_s^{SBI**}(t)$ based on $u(t) = \frac{1}{2}\left[u^{**}(t) + u^*(t)\right]$;
  4. Re-solve the linear equations (36) and (37) for $u(t)$ and $T^f(t)$;
  5. Use $T^f(t)$ to solve expression (39) for $V(t)$;
  6. Time march to $t + \triangle t$ using RKF45 with relative tolerance 10^{-7};
  7. Update the state, and return to Step 1 to proceed further in time.

end

While in Algorithm 1 a single corrections step is described, further corrections may be used to improve the accuracy of the algorithm. However, further correction steps did not show any substantial improvements on the result to merit the computational cost.

3 Results

To demonstrate the capabilities of the proposed scheme we consider two different problems. In the first one, we verify the numerical scheme using the SCEC SEAS Benchmark Problem BP-1 (Erickson & Jiang, 2018). In the second one, we investigate sequence of earthquakes and aseismic slip on a fault embedded in a low-velocity zone (LVZ).

3.1 SCEC SEAS Benchmark Problem Verification

We verify the hybrid scheme quasi-dynamic formulation using the benchmark problem BP-1 from the SCEC SEAS Validation Exercise. This benchmark problem describes a 2-D anti-plane shear problem, in which there exists a vertical strike-slip fault in a homogeneous half-space (see Figure 2a). The fault friction is governed by the regularized rate and state friction model with the aging law. The rupture is driven by slow tectonic loading defined by a constant plate velocity V_p imposed at a depth below the fault segment W_f, this allows for the aseismic creep to penetrate into the fault and eventually cause rupture. The parameters of the simulation is summarized in Table 1.

In addition to a prescribed slip rate beneath the fault, a free surface lies at $z = 0$. The frictional parameters on the fault vary along the depth of the domain. The frictional properties within region $[0, H]$ are defined by $a{-}b < 0$, describing a velocity-weakening (VW) patch; with a velocity-strengthening (VS) patch for the region between $[H{+}h, W_f]$, and a linear transition of length h between the two. The domain of the problem is defined by $(x, y, z) \in (-\infty, \infty) \times (-\infty, \infty) \times (0, \infty)$. The hybrid setup for this verification exercise is illustrated in Figure 2a. The virtual strip is discretized using FEM and the exchange of boundary conditions occur at surfaces S^+ and S^-. The choice of the width of the FEM strip in this case is arbitrary since this is a homogeneous linear-elastic domain, and we will show that the results indeed do not depend on the location of this far-field boundary. The dimensions of the simulated problem will vary to include a finite depth L_z. To account for the free surface in the SBI formulation, we use the method of images and map the slip and the slip rate from the physical domain $[0,L_z]$ to $[-L_z,0]$ when conducting the Fourier space calculation. Accordingly, the spatial domain in the SBI is considered as $[-L_z,L_z]$.

Figure 3 shows a comparison of the results from the hybrid scheme with those of a pure SBI formulation similar to the one in (Lapusta et al., 2004). Figure 3a, 3b, and 3c illustrate the time history plots of the slip rate and shear traction at stations $z = 0$, 7.5, 17.5 km respectively. The results show excellent agreement between the SBI and hybrid solutions. Figure 4a shows the time history for the surface slip rate at two different levels of the discretization for hybrid scheme and demonstrates its convergence to the high resolution pure SBI solution as the mesh is refined.

A significant advantage of the hybrid method is its capability to truncate the domain without incurring any accuracy drawbacks from the virtual boundary. To be able to model this problem using a full finite element model would require a domain of 80 km × 80 km to ensure that the far field boundaries would not influence the fault behavior. However, in the hybrid scheme, the virtual boundary is chosen, arbitrarily, to be 0.5 km from the fault plane. Accordingly, within the FEM strip, we only need to discretize a domain of 80 km × 1 km. Although the problem under consideration is linear-elastic, it serves the purpose of validating the truncation efficiency of the hybrid scheme. When extrapolated to more complex scenarios, this efficient near-field truncation allows the finite element discretization to be limited within a small strip, leading to potential savings in both computational time and memory cost.

The coupling procedure between the FEM and SBI method is based on the communication of boundary conditions across the virtual boundaries. Ideally, the solution should not depend on the location of either surfaces. To verify this point, we consider varying the width of the FEM strip denoted as W_s. Figure 4b shows the time history of surface slip rate for two simulations, one with $W_s = 1$ km and another with $W_s = 10$ km. The results suggest there exists no dependence for the solution on the virtual strip thickness.

3.2 Fault Embedded in a Low-Velocity Zone

Numerous field observations indicate the existence of complex crustal structures with heterogeneous fault zones that evolve due to damage accumulation from repeated earthquakes. In particular, the so called low-velocity fault zones (LVFZs) exist in most mature faults. Within these zones, the wave velocity is estimated to be reduced by 20 to 60 % relative to the host rock (Huang et al., 2014, 2016). The contrast may impact the long-term behavior of the earthquake cycles, resulting in complex patterns, as well as an increase in the slip due to the added compliance of these low-velocity regions.

To demonstrate the merit of the hybrid scheme developed in Section 2 and verified in Section 3.1, we consider a variation on the theme of the problem outlined in SCEC SEAS BP-1. Here, the rate and state fault is embedded in a LVFZ with varying material properties. Figure 2b demonstrates the hybrid setup specialized for low-velocity fault zones. The low-velocity zone may be viewed as a damaged region surrounding the fault with rigidity μ_D, shear velocity c_s^D, and half width W; sub- and superscript D will be used to describe properties within the LVFZ.

Three different rigidity contrasts μ_D/μ are considered: 80%, 60%, and 40%. The host rock is assumed to have a fixed shear modulus of 33 GPa. To account for the impact of the LVFZ width, several cases within each contrast is considered. We note that the width of the virtual strip may be taken equal to the width of the LVFZ, that is $W = W_s/2$. However, in our analysis, we introduced a buffer zone between the boundary of the LVFZ and the virtual strip boundaries S^+ and S^-. To make sure that the solution is independent of the buffer zone dimension, we have checked the results for various buffer zone thicknesses and obtained identical results. Except for the introduction of the LVFZ, all parameters used in the problem setup for this study is based on the SCEC SEAS benchmark exercise summarized in Table 1.

To facilitate the comparison between different cases, we utilize the dimensionless parameters μ_D/μ and W/h^*. Here, h^* represents the estimated nucleation length of the layered media. The nucleation length estimate in expression (28) predicts the nucleation size based on a fault embedded in a homogeneous medium. The introduction of LVFZ changes the nucleation size such that we recover the nucleation size of an undamaged homogeneous media h^*_{hom} in the limit $W \to 0$ but recover the nucleation size of a damaged homogeneous media h^{*D}_{hom} in the limit $W \to \infty$. To ensure accuracy and consistency it is thus crucial to identify the variation in nucleation size and resolve the mesh accordingly. (Kaneko et al., 2011) provided the following estimate for the nucleation size in this case based on linear stability analysis of a rate and state fault embedded in a layered medium.

$$h^* \tanh\left[W\frac{\pi}{2h^*} + \tanh^{-1}\left(\frac{\mu_D}{\mu}\right)\right] = h^{*D}_{hom} \tag{40}$$

We solve the above equation numerically and use the resulting estimate to normalize the width of the LVFZ.

3.2.1 Mild Rigidity Contrast: $\mu_D/\mu = 0.8$

In this section, we consider a LVFZ with mild contrast between the damaged media and the host rock. We compare the earthquake sequence for two cases: a case with LVFZ of width ratio $W/h^* = 0.17$, and a case with a homogeneous bulk and width ratio $W/h^* = 0$. Figure 5 shows the variation in surface slip rate profiles between the two cases. Since the rigidity varies mildly, the two solutions are similar with minor variations in the peak slip rate and inter-event time.

To get further insights into the impact of the LVFZ on the earthquake sequence, Figure 6a shows that with varying the width of the LVFZ, W, the characteristics of the earthquake sequence changes, including the peak slip rate, and inter-event time.

For example, Figure 6b suggests that the peak slip rate increases as the LVFZ width increases. The rate of change of the peak slip rate with width is high at small widths and becomes negligible in the limit of large LVFZ widths. In the current framework, this behavior may be explained by considering the following estimate for the slip rate based on fracture mechanics $V \propto \triangle\tau c_R/\mu$, where c_R is the rupture velocity. Thus, the velocity depend on the stress drop $\triangle\tau$, the rupture speed and the shear modulus. The current choice of the radiation damping term ensures that the rupture speed is bounded by the shear wave speed which in turn is proportional to the square root of the shear modulus (Rice, 1993). Thus, $V \propto \triangle\tau/\sqrt{\mu}$. As the width of the LVFZ increases, the effective shear modulus, on short wavelengths relevant to the crack tip propagation, decreases and eventually saturates at the value corresponding to the compliant region. The stress drop, however, remains almost invariant since it is constrained by the rate and state friction law which is weakly sensitive to variations in slip rate (the stress drop may slightly increase as the velocity increases, due to the logarithmic nature of the rate and state friction law). It follows that $V \propto 1/\sqrt{\mu_{eff}}$ where, μ_{eff} is the effective shear modulus over short wavelengths comparable to the process zone. As the width of the LVFZ increases from zero to the order of the process zone, the effective shear modulus rapidly decreases and the variation in the peak slip rate is more pronounced. As the width increases further to multiples of that length scale, the effective shear modulus approaches a constant value and the peak slip rate effectively saturates.

Furthermore, Figure 6c shows the non-monotonic dependence of the steady-state inter-event time T_c on the widths of the LVFZ W. Initially with the introduction of the LVFZ, a reduction in inter-event time is observed. The initial drop in the inter-event time may be associated with the reduction in the nucleation size due to the introduction of LVFZ. Thus the instability may be achieved faster as a smaller length scale needs to be destabilized. However, this pattern does not persist and is eventually reversed with larger-widths LVFZ showing longer inter-event times. This increase in the inter-event time may be explained by identifying that the loading of the fault is being applied through a constant plate loading rate imposed on a softer medium when the LVFZ is present. The stressing rate drops as the rigidity of the bulk drops. The effective rigidity of the medium, over long wavelengths relevant to the slow tectonic loading, decreases as the width of the LVFZ increases. The corresponding reduction in the stressing rate implies that it takes a longer time to accumulate the same amount of stress required for initiating the instability with the increased width of the LVFZ. In a simple quasi-dynamic model one would except that inter-event time is inversely proportional to the stressing rate, that is $T_c \propto 1/\dot{\tau}$.

3.2.2 Intermediate Rigidity Contrast: $\mu_D/\mu = 0.6$

Here, we consider a LVFZ with a material contrast of $\mu_D/\mu = 0.6$ and different values of W/h^*. Figure 7a demonstrates that by introducing a wide enough LVFZ, the resultant sequence of events may vary significantly. Specifically, the surface slip rate is compared for the following three cases: (1) homogeneous medium without damage, (2) a small LVFZ width with $W/h^* = 0.04$ and (3) a slightly wider LVFZ with $W/h^* = 0.08$. Results for cases (1) and (2) are almost identical with just a minor variation in the inter-event time and the peak slip rate. However, as the width of the LVFZ W/h^* further increases, as in case (3), the results qualitatively change. In particular we observe a kink in the surface slip rate profile that represent a transient acceleration that did not fully develop into a seismic phase which is emphasized in Figure 7b. This feature corresponds to the the emergence of sub-surface events, in which the rupture does not propagate all the way to the free surface. As a result, this event causes an increase in the shear stress and slip rate at the free surface, which is high compared to the background plate loading rate but still much lower than the seismic slip rate. In the following discussion we will use the term "surface reaching event" to describe an event in which the rupture propagates all the way to the free surface, while "sub-surface events" will be used to describe those that do not reach the free surface.

Figure 8a shows the peak slip rate as a function of time for a number of cases corresponding to different normalized widths of the LVFZ. Most notably, the sequence of events suggests non-monotonic complex patterns as the width of the LVFZ increases. On one hand, for a small width $W/h^* = 0.04$, the pattern is periodic and the inter-event time is uniform. On the other hand, if the width of the LVFZ is large enough ($W/h^* = \infty$), the sequence converges to a repeating pattern of alternating surface reaching and sub-surface events. Bridging the two limits, for intermediate widths of the LVFZ $W/h^* = 0.09$ (as shown in Figure 7b), the long-term response converge to a pattern of two surface reaching events, and a subsequent sub-surface event. The sub-surface event is characterized by a front that emerges in the VW region with the same nucleation size as the other events; yet since it never reaches the free surface, the maximum slip rate is not as large as the surface reaching events. It is also observed that following a sub-surface event, the subsequent surface reaching event is delayed. In Appendix A, we show examples of slip evolution in some of the cases discussed here which further suggest that the sub-surface event causes a slip deficit which leads to an increase in slip in the subsequent surface reaching event.

Figure 9 summarizes how the peak slip rate and the inter-event time vary as a function of the normalized widths for the different patterns investigated in this study. As discussed previously for the case of mild rigidity contrast, the general trend is that the peak slip rate increases as the width of the low-velocity zone increases as shown in Figure 10a. However, unlike the case of mild rigidity contrast, there is a considerable complexity in the inter-event time pattern. There is a transition from a single period at small widths, to triple periods at intermediate widths, to single periods as the width is further increased, and eventually settling into a double period pattern in the limit of homogeneous medium with a shear modulus equal to that of the LVFZ. As discussed previously, some of the events in the more complex sequences stop before reaching the surface and thus events within these periodic clusters are not identical. Furthermore, we observe that the general trend of increasing peak slip rate is not observed in cases with larger LVFZ width $W/h^* = 0.65{-}1$. Since these events are associated with successive surface reaching events, this deviation emerge due to the lack of residual stress concentration from a preceding sub-surface event. Thus, the peak slip rate values are lower than intermediate LVFZ cases with $W/h^* = 0.1 - 0.45$ where sub-surface events are observed, but still higher than in the homogeneous case.

To gain further insights into the characteristics of these alternating surface reaching and sub-surface events, we investigate the spatio-temporal evolution of the fault shear stress. Figure 10 shows snapshots of the shear stress τ along the fault surface before, during, and after both types of events for the case with $W/h^* = 0.09$. Prior to either event there is only stress concentration due to the inter-seismic slip backing beyond the VS-VW transition region into the VW region. Figure 10b shows that the event nucleates behind the region with stress concentration. The nucleation size is about $h^* = 1.54$km which is in line with the estimated size of $h^*_{est} = 1.51$ km from expression (40), indicating that both small and surface reaching events have approximately the same nucleation size.

The instability results in two propagating fronts, one expanding in the direction of the free surface and the other in the direction of the VS region with the VS region acting as a barrier to the rupture as shown in Figure 10c-f. Figure 10g shows that in the case of the sub-surface event the expanding rupture slows down as it propagates further in the VW region till it finally arrests before reaching the free surface. However, this premature arrest results in a residual stress concentration in the arrest region that would facilitate the propagation of subsequent surface reaching events as demonstrated by the stress profile 10 years after the sub-surface event in Figure 10h. The sub-surface event results in a lower average shear stress below the arrest region between $7{-}14$ km, explaining why following the sub-surface event, a delay in the occurrence of the next surface reaching event is observed.

The nucleation process for both the sub-surface and surface reaching events is illustrated in Figures 11a-b, which shows the slip rate versus the depth normalized by the estimated nucleation size. The nucleation size observed numerically is in excellent agreement with the theoretical estimate from expression (40) and is similar for both events. There exists some minor variation in the detailed distribution of the slip rate within the nucleation profile but the overall pattern is the same. The evolution of the peak slip rate in Figure 11c suggests that the surface reaching event experiences a slower increase in the peak slip rate and a slightly longer time to instability during the nucleation process.

3.2.3 *Strong Rigidity Contrast:* $\mu_D/\mu = 0.4$

Figure 12a shows the surface slip rate as a function of time, demonstrating that the complexity observed in Section 3.2.2 still occurs for the larger material contrast. In particular, we still observe for some cases a kink in the surface slip rate profile that represents a transient acceleration which did not fully develop into a seismic phase (as shown in Figure 12b) . This feature corresponds to the emergence of sub-surface events, in which the rupture does not propagate all the way to the free surface. Furthermore, for the cases considered, the sequence of events follows a non-monotonic complex pattern.

Figure 13 elaborates further on this non-monotonicity. Figure 13a shows that initially at smaller W/h^* the response is composed of periodic clusters of three events: two surface reaching events with a sub-surface event in between. However, when the W/h^* increases and the domain becomes more compliant, the behavior shifts to a single surface reaching event and a sub-surface event as illustrated in Figures 13b-c. At an intermediate $W/h^* = 0.7$ (shown in Figure 13d), a single periodic event is observed with only surface reaching events. At large width $W/h^* = 1.5$, the steady state response consists of clusters of two events: one surface reaching and one sub-surface but with different inter-event times compared to Figures 13b-c. We note that different models take different times to lose their memory of the initial conditions until they reach the statistical steady-state discussed here. Figure 13(a-d) shows small perturbation in the slip rate that manifest during inter-seismic period, yet fails to produce an instability. These transient accelerations in aseismic slip will be a focus of future investigations.

Figure 14 summarizes the main characteristics of the sequence of events. The overall arching slip rate amplification is still observed (as shown in Figure 14a), except for the case of $W/h^* = 0.7$. While for this case the slip rate is still higher than in the homogeneous case, the slip rate is slightly lower than the values observed at a lower LVFZ width. Since the sequence of events for this specific case consist of successive surface reaching events, this discrepancy may be attributed to the lack of residual stress concentration from sub-surface events that would yield a higher slip rate in the surface reaching events. In regards to the inter-event time shown in Figure 14b we observe a complex pattern. There is a transition from single-period events, to triple period events, to double periods then single periods again. Eventually double period events emerge as the width of the LVFZ goes to infinity. Interestingly, we also observe consistently that the inter-event time between the sub-surface event and the surface reaching event shrinks as W/h^* increase. However, the inter-event time between the surface reaching event and the subsequent sub-surface event increases as W/h^* increase. If we consider the cases of two surface reaching events between $\mu_D/\mu = 0.4$ and $\mu_D/\mu = 0.6$, the inter-event times fall within the same range even though W/h^* is smaller.

4 Discussion

In this paper, we have proposed a computational framework for modeling the quasi-dynamic sequence of earthquake and aseismic slip in an accurate and computationally efficient way without the need to fully discretize the entire domain of the problem. Specifically, we have introduced a hybrid scheme, coupling the finite element method (FEM) and the spectral boundary integral method (SBI) in a 2-D anti-plane setting. The proposed framework is capable of simulating the long-term history of seismic and aseismic slip on a vertical fault embedded in a heterogeneous medium with a free surface. Our approach resolves the various temporal scales associated with the inter-seismic slip and instability nucleation, dynamic rupture propagation, and post-seismic relaxation. During the dynamic rupture, the inertia terms were approximated using a radiation damping term (Rice, 1993). We then verified the proposed approach using the SCEC SEAS BP-1 benchmark (Erickson & Jiang, 2018), revealing an excellent agreement between the proposed technique and the well-established pure SBI approach. Furthermore, we demonstrated that the accuracy of the solution is independent of the FEM domain thickness, due to the exact nature of the truncation of the elastic fields being provided by the SBI formulation. Using the verified formulation, we investigated the evolutionary dynamics of a vertically dipping fault embedded in a low-velocity fault zone (LVFZ) of varying thickness and bulk properties.

A main advantage of the proposed approach is the ability of domain truncation, while retaining the independence of solution from the far-field boundary condition; thus, the solution is impartial to the FEM domain dimension. This allows for a reduction in the spatial discretization of the full domain to a small area of interest. The reduction in size translates to a small system of equations for bulk displacement, yielding significant reduction in the computational cost. The small linear system can be efficiently solved using direct solvers, circumventing the need for the choice of a proper preconditioner (Heinecke et al., 2014), which is a computational bottleneck when it comes to solving this class of problems using a purely domain based approach. Along the same lines, further mesh refinement is possible without the scaling complexities associated with a bigger domain; thus, allowing for explicit representation of extreme heterogeneities and potential other bulk nonlinearities with high resolution. Furthermore, the hybrid scheme utilizes a spectral representation of the boundary integral scheme to transform the nonlocal boundary conditions in space to local ones in the Fourier domain. This account for further computational savings. The truncation of the domain in the hybrid scheme accounts for savings in the overall run time, as well as memory utilization, as demonstrated in earlier studies (Ma et al., 2019). It is noted that the correction steps involved in the proposed algorithm incur additional computation cost; however, the cost is far less than the cost associated with modeling the entire domain.

Field observations have shown that faults are usually embedded in LVZs, in which the fault is surrounded by damaged rocks that are softer than the host rock material. LVFZs are usually several hundreds of meters wide, and may have significant reduction in seismic wave velocities (Yang & Zhu, 2010; Li et al., 2004). Several studies have considered LVFZ in terms of theoretical investigations of rupture nucleation (Ampuero et al., 2002), and computational modeling of dynamic ruptures (Brietzke & Ben-zion, 2006; Ben-Zion, 2002), but few have considered the problem of modeling earthquake cycles in the presence of this class of bulk heterogeneity. (Huang & Ampuero, 2011) have demonstrated the role the LVFZ plays during a single dynamic rupture event showing pulse like rupture. (Ma & Elbanna, 2015) showed that near fault low-velocity elastic inclusions alters the conditions for supershear propagation enabling supershear ruptures to occur at a much lower stress than required in homogeneous media. (Kaneko et al., 2011) developed an alternating quasistatic-dynamic scheme and focused on earthquake cycle simulation for faults embedded within a LVFZ. However, the study was limited to sequence of small repeating earthquakes, within a smaller scale problem considering only one level of material contrast between the LVFZ and the surrounding host rock. In our investigation, despite focusing on quasi-dynamic simulations, we have taken advantage of the hybrid scheme to study a larger length scale with a wider variety of material properties.

Our investigation for the low-velocity fault zone has revealed several interesting characteristics. For example, at small LVFZ material contrast $\mu_D/\mu = 0.8$, it was observed that the peak slip rate for successive events would increase with the increase of the normalized width of the low-velocity zone W/h^*. We have also observed that at larger widths of the LVZ, the time between subsequent events increase. Both observations are consistent with results from (Kaneko et al., 2011), suggesting that they are intrinsic in the nature of the LVZ and less sensitive to the inertia effects during dynamic rupture. Furthermore, in the quasi-dynamic limit considered here, and at larger material contrast, our results indicate the emergence of alternating sub-surface and surface reaching events. These sub-surface events contribute to a delay in the occurrence of the following surface reaching event. These results are in line with some field observations in which earthquakes fail to penetrate the Earth surface (Hartzell & Heaton, 1983).

Moreover, the earthquake cycle complexity in which sub-surface events emerge is shown to be directly correlated to the compliance of the LVFZ. The study of the nucleation process for both surface reaching and sub-surface events demonstrated that the nucleation size of both events is very similar. However, we observed some minor variation in terms of depth and slip rate profile. This observation is consistent with findings in (Lapusta & Rice, 2003), which suggested the emergence of small event complexity in a homogeneous medium as the length scale parameter in the rate and state friction law decreases, leading to a reduction in the nucleation size, but stated that both large and small events have similar nucleation characteristics. While the effective nucleation size decreases due to the introduction of a LVFZ, our findings suggest that the nucleation size is not entirely the determining factor as such complexity is not obvious for cases with the same W/h^* but different rigidity contrast. If the nucleation size was the only factor, we would expect the greatest complexity to emerge in the case of $W \to \infty$ which has the smallest nucleation size. However, we observe that LVFZ with small to intermediate W/h^* ratios may show a richer behavior indicating that the rigidity contrast plays a critical role in promoting complexity, in addition to the reduced nucleation size. Furthermore, while sub-surface and surface reaching events do appear in the limit of $W/h^* \to \infty$, the sequence pattern is completely different than in the intermediate thickness cases.

Within a specific parameter space, it is observed that the sequence of earthquakes may vary drastically, from a sequence of single periodic events to a pattern of repeating event clusters. The pattern may be either a sequence of one sub-surface event followed by a surface reaching event or one sub-surface event followed by two surface reaching events. The pattern of events also follows a non-monotonic trend. For example, at $\mu_D/\mu = 0.6$ we observe that at low W/h^*, the sequence of events start as single successive events. However, with the increase of W/h^*, the pattern shifts to a triple-event cluster. Finally, at $W = \infty$, the pattern converge to a cluster of two events. Overall, we found that the introduction of LVFZ contribute to an increase in the maximum peak slip rate within the earthquake sequence particularly as the rigidity contrast increases. The peak slip rate generally increases with respect to the homogeneous host rock case as the width of the LVFZ increases, with some minor fluctuations depending on the details of the seismic sequence.

While the proposed hybrid scheme offers a step toward computationally efficient and accurate methodologies for including fault zone complexities within earthquake cycle simulations, the method as presented here has some limitations. Most notably, in the proposed scheme we have opted to disregard the inertia terms and instead employ the radiation damping approximation. While this approach gives grave insight on the nucleation and inter-seismic response of the earthquake cycle, it lacks in consideration the substantial role of inertia during the dynamic rupture process. The radiation damping correction used here only approximates this inertia effect, but it was shown previously, at least in the framework of planar faults in homogeneous media, that some differences in the characteristics of earthquake sequence may be observed between dynamic and quasi-dynamic simulations (Thomas et al., 2014). (Hajarolasvadi & Elbanna, 2017) and (Ma et al., 2019) have considered dynamics within the same hybrid framework for a single dynamic rupture event and demonstrated that the results obtained match perfectly with FEM within anti-plane and in-plane 2-D settings but at a fraction of computational cost. Thus, the next natural step for the current SEAS implementation would be to extend it to include inertial dynamics. This will be further explored in future investigations.

It should be noted that even though we are using a quasi-dynamic approximation, several other studies indicate that some of the features observed in the current models mimic those happening in a fully dynamic simulation. For example, (Lapusta et al., 2004) demonstrated that sequence of small and large events would still occur in dynamic systems with small nucleation size. A more relevant observation to the quasi-dynamic limit that is common between this current study and (Lapusta & Rice, 2003) is that the nucleation process for both small and large events is similar. Similarly, (Kaneko et al., 2011) also demonstrated that amplification in the slip rate and increase in inter-event time is proportional to W/h^* for $\mu_D/\mu = 0.6$ within a dynamic framework for the co-seismic phase, which is also observed in the current study.

In this work, we have focused on modeling planar faults as an initial step. However, the hybrid scheme can fully accommodate non-planar fault setups, as well as other complex fault zone topologies including fault branches (Ma & Elbanna, 2019). Furthermore, the Galerkin finite element approach used in the current study may be replaced by any other domain-based model. For example, if we want to relax the constraint that the fault location is known apriori, a more flexible approach would be to adopt a discretization approach that readily accounts for discontinuities such as generalized finite element method (F. Liu & Borja, 2009), or discontinuous Galerkin methods (Pelties et al., 2012), or phase field model (Miehe et al., 2010), which would further enable arbitrary growth of fault surfaces, as well as nucleation and growth of new surfaces. Furthermore, the FEM may be replaced by a discrete element method (Herrmann et al., 1998) or smooth particle hydrodynamics formulation (Bui et al., 2008) to enable explicit incorporation of fault gouge dynamics. The proposed hybrid scheme is general enough to work with any of those approaches, and we plan to explore these implementation in the future.

In this paper, we have limited our investigation to modeling sequence of earthquakes and aseismic slip in linearly elastic heterogeneous domains undergoing anti-plane deformations. However, as demonstrated in (Hajarolasvadi & Elbanna, 2017) and (Ma et al., 2019) the hybrid scheme may be readily extended to account for nonlinear bulk rheology as well as 2-D in plane setting with complex fault topology. Extension to 3-D setups with nonlinear constitutive laws is also straightforward. By enlarging the scope of our investigations to these new directions, this would potentially provide more insight on the role of various forms of fault zone complexities, including topological, geometrical, and rheological nonlinearities, on the spatio-temporal evolution of seismicity.

5 Conclusion

In this paper, we present a hybrid framework that couples finite element method with spectral boundary integral method to conduct earthquake cycle simulations, and investigate the influence of material heterogeneities on the behavior of the earthquake sequence and aseismic slip. Such simulations incur substantial computational cost on domain based approaches, as the material heterogeneity or nonlinearity impose restrictions on the resolution of the mesh. A verification exercise demonstrates the accuracy of the scheme, which we then utilize to study the response of faults embedded within a low-velocity zone. The results shows the importance of off-fault properties on the earthquake sequence. The main conclusions may be summarized as follows:

- The proposed scheme matches other well-established numerical methods in the limit of a homogeneous medium. This comes at a fraction of the cost that other domain-based approaches would incur.
- The low-velocity fault zone contributes to a change in the overall properties of the earthquake cycle
- Should the low-velocity fault zone be sufficiently compliant, the results show the emergence of sub-surface events that fail to penetrate to the free surface.
- The sub-surface and surface reaching events share similar nucleation size; however, the sub-surface event results in a residual stress concentration that contributes to a higher peak slip rate.
- Event pattern and LVFZ W/h^* are non-monotonously related, in which we observe transitions from single periods to triple periods, and again to single or double periods as W/h^* increase.

Appendix A: Cumulative Slip Profile

Figure A1 shows the cumulative slip profile with different earthquake sequence pattern for three cases of LVFZ with different widths W. The blue solid lines are plotted every five years and show the inter-seismic creep starting in the velocity-strengthening region and penetrating into the velocity-weakening region. The quasi-dynamic rupture is shown with dashed red lines and plotted every one second. Figure A1a shows the sub-surface events that fail to propagate to the free surface. Furthermore, we observe a significant slip accumulation during the subsequent surface reaching event. This is due to the slip deficit that accumulates at the surface from the sub-surface ruptures which is compensated for by the increased slip in the subsequent surface reaching event. Figure A1b show the earthquake sequence for a case with $W/h^* = 0.65$, resulting in periodic successive surface reaching events. Interestingly, in this case the rupture decelerates over the deeper half of the fault and then appears to accelerate again. This is further discussed shortly. The limit of a homogeneous case with $\mu = 19.8$ GPa is demonstrated in Figure A1c, where sub-surface events are followed by surface reaching ones.

To elaborate further on the deceleration observed in Figure A1b, we show in Figure A2 the snapshots of the slip rate during one of the surface reaching events. A sharp decrease in the slip rate is observed near the VS region as the rupture propagates toward the free surface. After a few seconds, we observe a re-acceleration in this region due to another growth of instability along the fault line in Figure A2h. To further explore this phenomenon, Figure A3 shows the evolution of the slip rate along the fault depth for the time period between 33 and 39 seconds. The figure illustrates the emergence of rapid back propagating fronts associated with unstable growth of slip emanating in the vicinity of the region with steep gradient in the slip rate at the toe of the quasi-slip pulse observed in Figure A2g. Similar observations for the emergence of slip pulses and rapid back propagating fronts have been reported by (Idini & Ampuero, 2018) and warrants further investigations in the future.

Acknowledgment

This research has been supported by the National Science Foundation (CAREER Award Number 1753249) and the Southern California Earthquake Center through a collaborative agreement between NSF. Grant Number: EAR0529922 and USGS Grant Number: 07HQAG0008. Additional funds for investigation of low velocity fault zones were provided by the Department of Energy under Award Number DE-FE0031685. This work was prepared as an account of work sponsored by an agency of the United States Government. Neither the United States Government nor any agency thereof, nor any of their employees, makes any warranty, express or implied, or assumes any legal liability or responsibility for the accuracy, completeness, or usefulness of any information, apparatus, product, or process disclosed, or represents that its use would not infringe privately owned rights. Reference herein to any specific commercial product, process, or service by trade name, trademark, manufacturer, or otherwise does not necessarily constitute or imply its endorsement, recommendation, or favoring by the United States Government or any agency thereof. The views and opinions of authors expressed herein do not necessarily state or reflect those of the United States Government or any agency thereof.

References

Aagaard, B. T., Knepley, M. G., & Williams, C. A. (2013). A domain decomposition approach to implementing fault slip in finite-element models of quasi-static and dynamic crustal deformation. *Journal of Geophysical Research: Solid Earth*, *118*(6), 3059–3079. doi: 10.1002/jgrb.50217

Aliabadi, M. H. (2009). Boundary Element Formulations in Fracture Mechanics. *Applied Mechanics Reviews*, *50*(2), 83. doi: 10.1115/1.3101690

Ampuero, J. P., & Rubin, A. M. (2008, 1). Earthquake nucleation on rate and state faults - Aging and slip laws. *Journal of Geophysical Research: Solid Earth*, *113*(1). doi: 10.1029/2007JB005082

Ampuero, J.-P., Vilotte, J.-P., & Sánchez-Sesma, F. J. (2002). Nucleation of rupture under slip dependent friction law: Simple models of fault zone. *Journal of Geophysical Research: Solid Earth*, *107*(B12), 2–1. doi: 10.1029/2001jb000452

Ben-Zion, Y. (2002). Dynamic rupture on an interface between a compliant fault zone layer and a stiffer surrounding solid. *Journal of Geophysical Research*, *107*(B2). doi: 10.1029/2001jb000254

Ben-Zion, Y., Peng, Z., Okaya, D., Seeber, L., Armbruster, J. G., Ozer, N., … Aktar, M. (2003). A shallow fault-zone structure illuminated by trapped waves in the Karadere-Duzce branch of the North Anatolian Fault, western Turkey. *Geophysical Journal International*, *152*(3), 699–717. doi: 10.1046/j.1365-246X.2003.01870.x

Ben-Zion, Y., & Rice, J. R. (1996). *Slip complexity in earthquake fault models* (Vol. 93; Tech. Rep.).

Berenger, J.-p. (1994). A Perfectly Matched Layer for the Absorption of Electromagnetic Waves_Jean Pierre Berenger.pdf. , *200*, 185–200.

Bettess, P. (1977). Infinite elements. *International Journal for Numerical Methods in Engineering*, *11*(1), 53–64. Retrieved from `http://doi.wiley.com/10.1002/nme.1620110107` doi: 10.1002/nme.1620110107

Breitenfeld, M. S., & Geubelle, P. H. (1998). Numerical analysis of dynamic debonding under 2D in-plane and 3D loading. *Recent Advances in Fracture Mechanics*, 13–37. doi: 10.1007/978-94-017-2854-6{_}2

Brietzke, G. B., & Ben-zion, Y. (2006). Examining tendencies of in-plane rupture to migrate to material interfaces. *Geophysical Journal International*, *167*(2), 807–819. doi: 10.1111/j.1365-246X.2006.03137.x

Bui, H. H., Fukagawa, R., Sako, K., & Ohno, S. (2008, 8). Lagrangian meshfree particles method (SPH) for large deformation and failure flows of geomaterial using elastic-plastic soil constitutive model. *International Journal for Numerical and Analytical Methods in Geomechanics*, *32*(12), 1537–1570. Retrieved from `http://doi.wiley.com/10.1002/nag.688` doi: 10.1002/nag.688

Chester, F. M., Evans, J. P., & Biegel, R. L. (1993). Internal structure and weakening mechanisms of the San Andreas Fault. *Journal of Geophysical Research*, *98*(B1), 771–786. doi: 10.1029/92JB01866

Cochran, E. S., Li, Y. G., Shearer, P. M., Barbot, S., Fialko, Y., & Vidale, J. E. (2009). Seismic and geodetic evidence for extensive, long-lived fault damage zones. *Geology*, *37*(4), 315–318. doi: 10.1130/G25306A.1

D'Amico, S. (2016). *Earthquakes and Their Impact on Society* (S. D'Amico, Ed.). Cham: Springer International Publishing. Retrieved from `http://link.springer.com/10.1007/978-3-319-21753-6` doi: 10.1007/978-3-319-21753-6

Day, S. M., Dalguer, L. A., Lapusta, N., & Liu, Y. (2005). Comparison of finite difference and boundary integral solutions to three-dimensional spontaneous rupture. *Journal of Geophysical Research: Solid Earth*, *110*(12), 1–23. doi: 10.1029/2005JB003813

Dieterich, J. H. (1979). Modeling of rock friction 1. Experimental results and constitutive equations. *Journal of Geophysical Research: Solid Earth*, *84*(B5), 2161–2168. doi: 10.1029/JB084iB05p02161

Dieterich, J. H. (1992). Earthquake nucleation on faults with rate-and state-dependent strength. *Tectonophysics*, *211*(1-4), 115–134. doi: 10.1016/0040-1951(92)90055-B

Erickson, B. A., & Day, S. M. (2016). Journal of Geophysical Research : Solid Earth Bimaterial effects in an earthquake cycle model using rate-and-state friction. , 2480–2506. doi: 10.1002/2015JB012470.Received

Erickson, B. A., & Dunham, E. M. (2014). An efficient numerical method for earthquake cycles in heterogeneous media: Alternating subbasin and surface-rupturing events on faults crossing a sedimentary basin. *Journal of Geophysical Research: Solid Earth*, *119*(4), 3290–3316. doi: 10.1002/2013JB010614

Erickson, B. A., Dunham, E. M., & Khosravifar, A. (2017). A finite difference method for off-fault plasticity throughout the earthquake cycle. *Journal of the Mechanics and Physics of Solids*, *109*, 50–77. Retrieved from `http://dx.doi.org/10.1016/j.jmps.2017.08.002` doi: 10.1016/j.jmps.2017.08.002

Erickson, B. A., & Jiang, J. (2018). *SEAS Benchmark Problem BP1.* Retrieved from `http://scecdata.usc.edu/cvws/seas/`

Geubelle, P., & Rice, J. R. (1995, 11). A spectral method for three-dimensional elastodynamic fracture problems. *Journal of the Mechanics and Physics of Solids*, *43*(11), 1791–1824. Retrieved from `https://linkinghub.elsevier.com/retrieve/pii/002250969500043I` doi: 10.1016/0022-5096(95)00043-I

Geubelle, P. H., & Breitenfeld, M. S. (1997). Numerical analysis of dynamic debonding under anti-plane shear loading. *International Journal of Fracture*, *85*(3), 265–282. doi: 10.1023/A:1007498300031

Hajarolasvadi, S., & Elbanna, A. E. (2017). A new hybrid numerical scheme for modelling elastodynamics in unbounded media with near-source heterogeneities. *Geophysical Journal International*, *211*(2), 851–864. doi: 10.1093/GJI/GGX337

Hartzell, S., & Heaton, T. (1983). Inversion of strong ground motion and teleseismic waveform data for the fault rupture history of the 1979 Imperial Valley, California, earthquake. *Bulletin of the Seismological Society of ...*, *73*(6), 1553–1583. Retrieved from `http://www.bssaonline.org/content/73/6A/1553.short`

Heinecke, A., Breuer, A., Rettenberger, S., Bader, M., Gabriel, A. A., Pelties, C., ... Dubey, P. (2014). Petascale High Order Dynamic Rupture Earthquake Simulations on Heterogeneous Supercomputers. *International Conference for High Performance Computing, Networking, Storage and Analysis, SC*, *2015-Janua*(January), 3–14. doi: 10.1109/SC.2014.6

Herrendörfer, R., Gerya, T., & van Dinther, Y. (2018, 6). An Invariant Rate- and State-Dependent Friction Formulation for Viscoeastoplastic Earthquake Cycle Simulations. *Journal of Geophysical Research: Solid Earth*, *123*(6), 5018–5051. doi: 10.1029/2017JB015225

Herrmann, H. J., Hovi, J.-P., & Luding, S. (Eds.). (1998). *Physics of Dry Granular Media*. Dordrecht: Springer Netherlands. Retrieved from http://link.springer.com/10.1007/978-94-017-2653-5 doi: 10.1007/978-94-017-2653-5

Hillers, G., Ben-Zion, Y., & Mai, P. M. (2006). Seismicity on a fault controlled by rate- and state-dependent friction with spatial variations of the critical slip distance. *Journal of Geophysical Research: Solid Earth*, *111*(1), 1–23. doi: 10.1029/2005JB003859

Huang, Y., & Ampuero, J. P. (2011). Pulse-like ruptures induced by low-velocity fault zones. *Journal of Geophysical Research: Solid Earth*, *116*(12), 1–13. doi: 10.1029/2011JB008684

Huang, Y., Ampuero, J. P., & Helmberger, D. V. (2014, 4). Earthquake ruptures modulated by waves in damaged fault zones. *Journal of Geophysical Research: Solid Earth*, *119*(4), 3133–3154. Retrieved from http://doi.wiley.com/10.1002/2013JB010724 doi: 10.1002/2013JB010724

Huang, Y., Beroza, G. C., & Ellsworth, W. L. (2016, 9). Stress drop estimates of potentially induced earthquakes in the Guy-Greenbrier sequence. *Journal of Geophysical Research: Solid Earth*, *121*(9), 6597–6607. Retrieved from http://doi.wiley.com/10.1002/2016JB013067 doi: 10.1002/2016JB013067

Idini, B. R., & Ampuero, J.-p. (2018). Rupture Complexity Promoted by Damaged Fault Zones in Earthquake Cycle Models. , *110*(2011), 10500080. doi: 10.5281/zen-odo.322459

J.R.Rice, & A.L.Ruina. (1983). Stability of Steady Frictional Slipping. *Journal of Applied Mechanics*, *105*, 343–349.

Kaneko, Y., Ampuero, J. P., & Lapusta, N. (2011). Spectral-element simulations of long-term fault slip: Effect of low-rigidity layers on earthquake-cycle dynamics. *Journal of Geophysical Research: Solid Earth*, *116*(10), 1–18. doi: 10.1029/2011JB008395

Kuna, M. (2013). *Finite Elements in Fracture Mechanics* (Vol. 201). Retrieved from http://link.springer.com/10.1007/978-94-007-6680-8 doi: 10.1007/978-94-007-6680-8

Lapusta, N., & Liu, Y. (2009). Three-dimensional boundary integral modeling of spontaneous earthquake sequences and aseismic slip. *Journal of Geophysical Research: Solid Earth*, *114*(9), 1–25. doi: 10.1029/2008JB005934

Lapusta, N., & Rice, J. R. (2003). Nucleation and early seismic propagation of small and large events in a crustal earthquake model. *Journal of Geophysical Research: Solid Earth*, *108*(B4), 1–18. doi: 10.1029/2001jb000793

Lapusta, N., Rice, J. R., Ben-Zion, Y., & Zheng, G. (2004). Elastodynamic analysis for slow tectonic loading with spontaneous rupture episodes on faults with rate- and state-dependent friction. *Journal of Geophysical Research: Solid Earth*, *105*(B10), 23765–23789. doi: 10.1029/2000jb900250

Lay, T. (2012). Seismology: Why giant earthquakes keep catching us out. *Nature*, *483*(7388), 149–150. doi: 10.1038/483149a

Lewis, M. A., & Ben-Zion, Y. (2010). Diversity of fault zone damage and trapping structures in the Parkfield section of the San Andreas Fault from comprehensive analysis of near fault seismograms. *Geophysical Journal International*, *183*(3), 1579–1595. doi: 10.1111/j.1365-246X.2010.04816.x

Li, Y.-G., Aki, K., Adams, D., Hasemi, A., & Lee, W. H. K. (2004). Seismic guided waves trapped in the fault zone of the Landers, California, earthquake of 1992. *Journal of Geophysical Research: Solid Earth*, *99*(B6), 11705–11722. doi: 10.1029/94jb00464

Liu, F., & Borja, R. I. (2009, 9). An extended finite element framework for slow-rate frictional faulting with bulk plasticity and variable friction. *International Journal for Numerical and Analytical Methods in Geomechanics*, *33*(13), 1535–1560. Retrieved from http://doi.wiley.com/10.1002/nag.777 doi: 10.1002/nag.777

Liu, Y., & Rice, J. R. (2007). Spontaneous and triggered aseismic deformation transients in a subduction fault model. *Journal of Geophysical Research: Solid Earth*, *112*(9), 1–23. doi: 10.1029/2007JB004930

Luo, Y., & Ampuero, J. P. (2018). Stability of faults with heterogeneous friction properties and effective normal stress. *Tectonophysics*, *733*(October 2017), 257–272. Retrieved from https://doi.org/10.1016/j.tecto.2017.11.006 doi: 10.1016/j.tecto.2017.11.006

Lyakhovsky, V., Ben-Zion, Y., Ilchev, A., & Mendecki, A. (2016). Dynamic rupture in a damage-breakage rheology model. *Geophysical Journal International*, *206*(2), 1126–1143. doi: 10.1093/gji/ggw183

Lysmer, O., & Kuhlemeyer, R. L. (1969). Finite Dynamic Model for Infinite Media. *Journal of the Engineering Mechanics Division, ASCE*, *95*(8), 859–869.

Ma, X., & Elbanna, A. E. (2015). Effect of off-fault low-velocity elastic inclusions on supershear rupture dynamics. *Geophysical Journal International*, *203*(1), 664–677. doi: 10.1093/gji/ggv302

Ma, X., & Elbanna, A. E. (2019). Dynamic Rupture Propagation on Fault Planes with Explicit Representation of Short Branches Dynamic Rupture Propagation on Fault Planes with Explicit Representation of Short Branches. *EarthArXiv*.

Ma, X., Hajarolasvadi, S., Albertini, G., Kammer, D. S., & Elbanna, A. E. (2019). A hybrid finite element-spectral boundary integral approach: Applications to dynamic rupture modeling in unbounded domains. *International Journal for Numerical and Analytical Methods in Geomechanics*, *43*(1), 317–338. doi: 10.1002/nag.2865

Miehe, C., Welschinger, F., & Hofacker, M. (2010, 9). Thermodynamically consistent phase-field models of fracture: Variational principles and multi-field FE implementations. *International Journal for Numerical Methods in Engineering*, *83*(10), 1273–1311. Retrieved from `http://doi.wiley.com/10.1002/nme.2861` doi: 10.1002/nme.2861

Nishioka, T., & Atluri, S. N. (1982). Numerical analysis of dynamic crack propagation: Generation and prediction studies. *Engineering Fracture Mechanics*, *16*(3), 303–332. doi: 10.1016/0013-7944(82)90111-4

Noda, H., & Lapusta, N. (2013). Stable creeping fault segments can become destructive as a result of dynamic weakening. *Nature*, *493*(7433), 518–521. Retrieved from `http://dx.doi.org/10.1038/nature11703` doi: 10.1038/nature11703

Okubo, P. G. (1989). Dynamic rupture modeling with laboratory-derived constitutive relations. *Journal of Geophysical Research*, *94*(B9), 12321. Retrieved from `http://doi.wiley.com/10.1029/JB094iB09p12321` doi: 10.1029/JB094iB09p12321

Pelties, C., De La Puente, J., Ampuero, J. P., Brietzke, G. B., & Käser, M. (2012). Three-dimensional dynamic rupture simulation with a high-order discontinuous Galerkin method on unstructured tetrahedral meshes. *Journal of Geophysical Research: Solid Earth*, *117*(2), 1–15. doi: 10.1029/2011JB008857

Rice, J. R. (1993). Spatio-temporal complexity of slip on a fault. *Journal of Geophysical Research*, *98*(B6), 9885–9907. doi: 10.1029/93JB00191

Rice, J. R. (2006). Heating and weakening of faults during earthquake slip. *Journal of Geophysical Research: Solid Earth*, *111*(5), 1–29. doi: 10.1029/2005JB004006

Ruina, A. (1983). Slip instability and state variable friction laws. *Journal of Geophysical Research*, *88*(B12), 10359–10370. doi: 10.1029/JB088iB12p10359

Shibazaki, B., & Matsu'ura, M. (1992, 6). Spontaneous processes for nucleation, dynamic propagation, and stop of earthquake rupture. *Geophysical Research Letters*, *19*(12), 1189–1192. Retrieved from `http://doi.wiley.com/10.1029/92GL01072` doi: 10.1029/92GL01072

Thomas, M. Y., Lapusta, N., Noda, H., & Avouac, J. P. (2014). Quasi-dynamic versus fully dynamic simulations of earthquakes and aseismic slip with and without enhanced coseismic weakening. *Journal of Geophysical Research: Solid Earth*, *119*(3), 1986–2004. doi: 10.1002/2013JB010615

Tse, S. T., & Rice, J. R. (1986). Crustal earthquake instability in relation to the depth variation of frictional slip properties. *Journal of Geophysical Research*, *91*(B9), 9452. doi: 10.1029/jb091ib09p09452

Urgen Bathe, K.-J. (2001). The infsup condition and its evaluation for mixed finite element methods. *Computers and Structures*, *79*(79), 243–252.

Y.-G. Li, & Leary, P. C. (1990). Fault zone trapped seismic waves. *Bulletin of the Seismological Society of Americ*, *80*(5), 1245–127.

Yang, H., & Zhu, L. (2010). Shallow low-velocity zone of the San Jacinto fault from local earthquake waveform modelling. *Geophysical Journal International*, *183*(1), 421–432. doi: 10.1111/j.1365-246X.2010.04744.x

Yang, H., Zhu, L., & Cochran, E. S. (2011). Seismic structures of the Calico fault zone inferred from local earthquake travel time modelling. *Geophysical Journal International*, *186*(2), 760–770. doi: 10.1111/j.1365-246X.2011.05055.x

1028 ## Tables

Parameter	Symbol	Value
Density (kg/m^3)	ρ	2670.0
Shear wave speed (km/s)	c_s	3.464
Effective normal stress on fault (MPa)	σ_n	50.0
Critical slip distance (m)	L	0.008
Plate rate (m/s)	V_p	10^{-9}
Reference slip rate (m/s)	V_o	10^{-6}
Initial slip rate (m/s)	V_{init}	10^{-9}
Reference fricition coefficient	f_o	0.6
Depth extent of uniform VW region (km)	H	15.0
Width of transition (km)	h	3.0
Rate and State parameter	b	0.015
Rate and State parameter	a_{max}	0.025
Rate and State parameter	a_{min}	0.010
Fault length (km)	W_f	40
Distance between two virtual boundaries (km)	W_s	1
Loading distance (km)	W_l	40
Depth (km)	L_z	80

Table 1: Problem parameters for the SCEC SEAS Benchmark BP1-2D

1029 # Figures

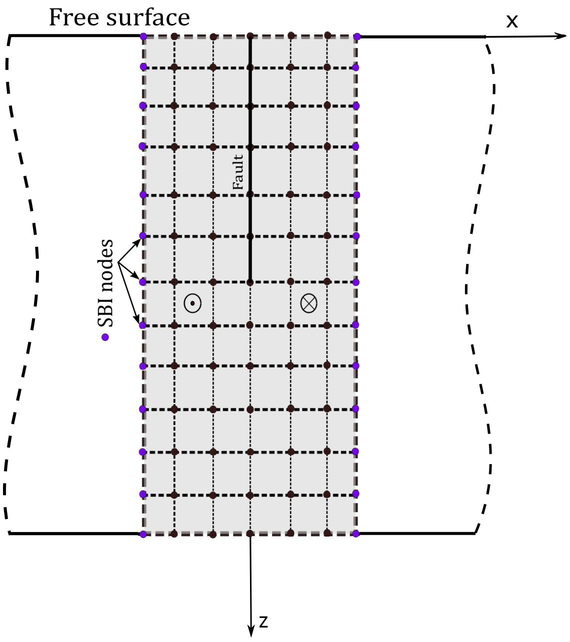

Figure 1: Illustration of the hybrid method with coupling of the FEM and SBI. A schematic illustration of the problem of our 2-D model, showing rate and state fault embedded in a heterogeneous sub-space subjected to anti-plane shear deformations. The balance equations within the region of interest are discretized with finite element model. The tractions on SBI nodes (blue) are computed using SBI scheme with known Green's function and applied on FEM (black) as traction boundary conditions on each side. The free surface presents a traction-free boundary condition.

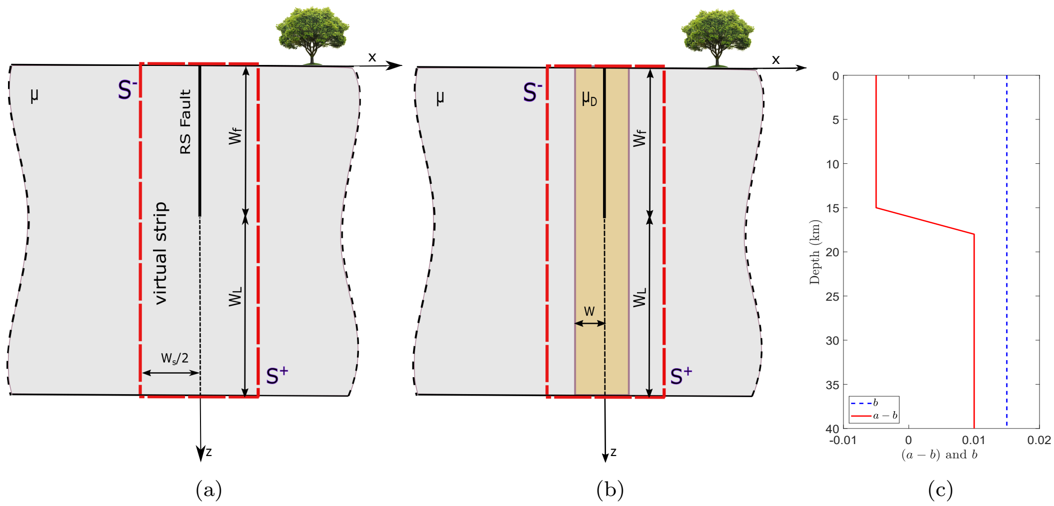

Figure 2: Problem setup. (a) The hybrid scheme setup for BP1-2D. The width of the finite element domain is W_s. The fault length is W_f. The loading is done beneath the fault at a rate V_p applied on length W_L. A planar fault is embedded in a homogeneous, linear-elastic half-space with a free surface. The fault creeps at an imposed plate rate of V_p down to infinite depth. (b) Low-velocity fault zone hybrid scheme setup, where the damaged region is confined within width W and has a shear modulus μ_D. The red box indicates the domain to be discretized using the FEM coupled with the SBI at the lateral boundaries. (c) The variability in the distribution of rate and state parameters $(a - b)$ and b for both problems.

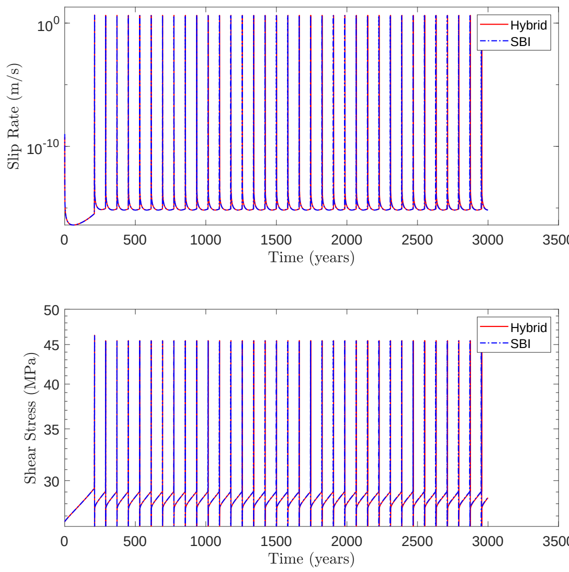

(a)

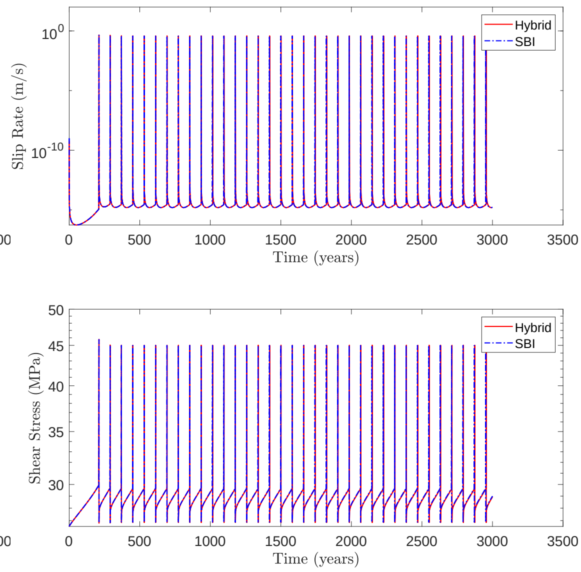

(b)

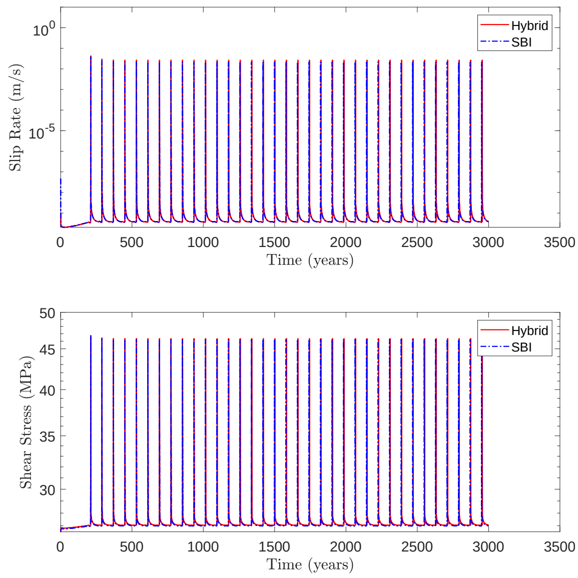

(c)

Figure 3: Results for SCEC SEAS Benchmark Problem BP-1 simulation comparing the hybrid method (in red) with the spectral boundary integral method (in blue). (a) Time history of the slip rate, and shear stress at the station on the free surface. (b) Time history of the slip rate, and shear stress at a station 7.5 km away from the free surface. (c) Time history of the slip rate, and shear stress at a station 17.5 km away from the free surface. All results show excellent agreement between the two methods.

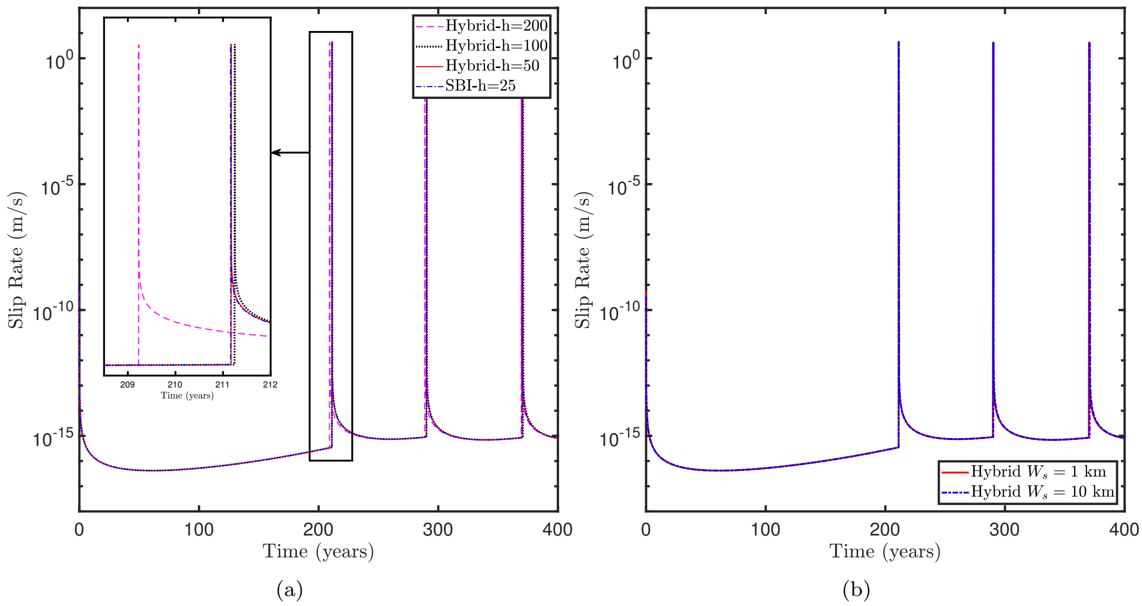

Figure 4: Convergence study for the hybrid scheme. (a) Surface slip rate on the fault as a function of time comparing the solution of the hybrid scheme against the pure SBI solution for various mesh sizes of FEM (h = 50 m, 100 m, and 200 m). The results from the hybrid scheme matches the SBI solution for both seismic and inter-seismic periods, and converge to the SBI solution with refinement. (b) A 400-year time history of the surface slip rate on the fault comparing two different FEM strip W_s thicknesses, 1 km and 10 km. The results from the two different widths show that the solution does not vary with increased thickness and is insensitive to the location of the virtual boundaries.

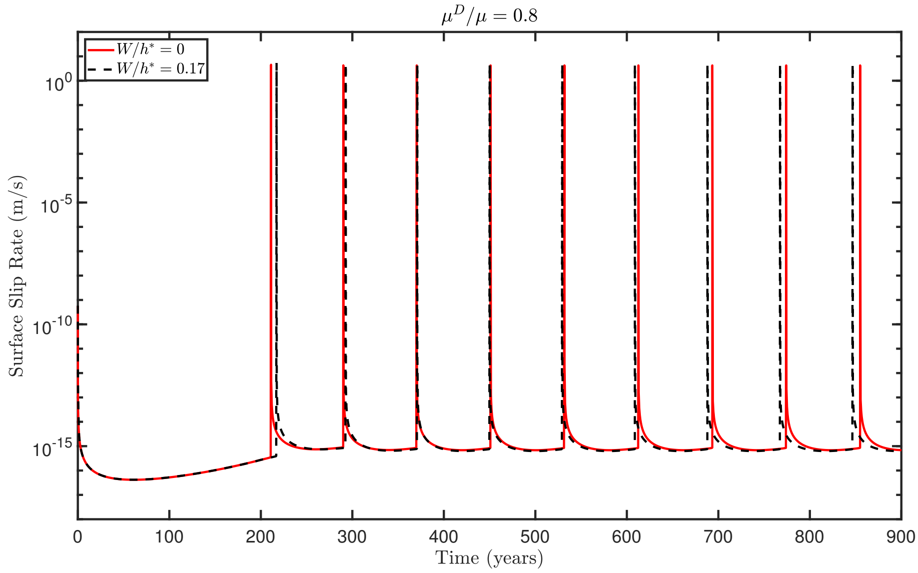

Figure 5: Surface slip rate history, illustrating the influence of a mild rigidity contrast on the earthquake sequence of the simulated problem. Shown are the results for the homogeneous case compared to the LVFZ with $W/h^* = 0.17$ and $\mu_D/\mu = 0.8$. The two cases show approximately the same trend.

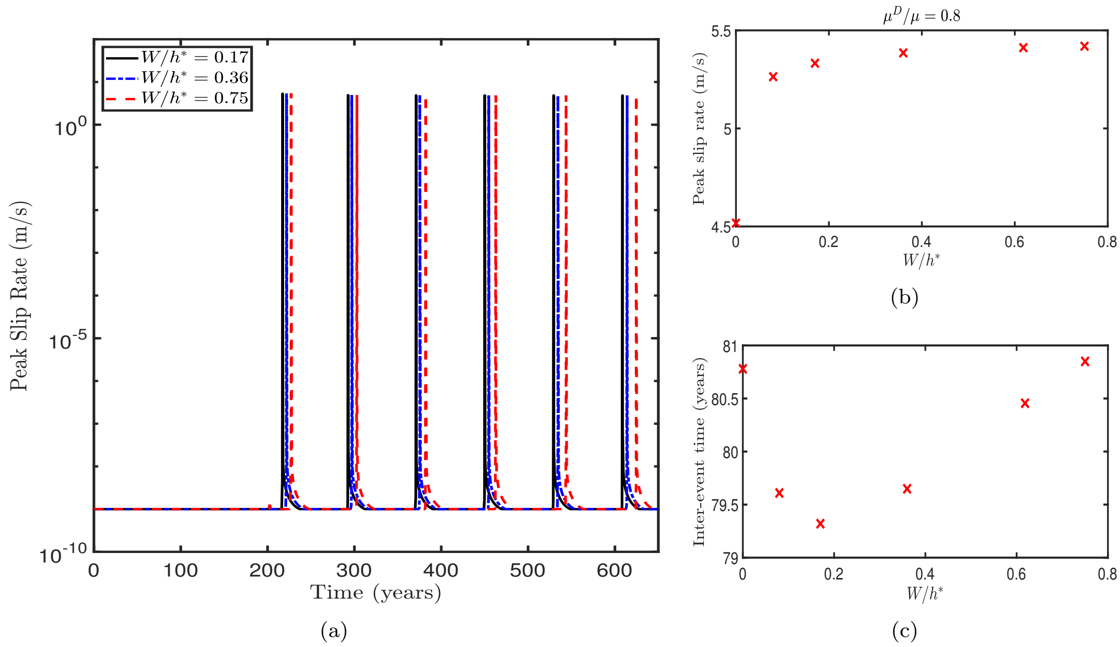

Figure 6: Effects of a low-velocity fault zone of width W on earthquake sequence. (a) Time history of peak slip rate demonstrating the shift in occurrence time for various LVFZ W/h^* at a mild rigidity contrast of $\mu_D/\mu = 0.8$. (b) The maximum peak slip rate during earthquake cycle as a function of W/h^*. The moderate amplification in peak slip rate is associated with the increase in W/h^*. (c) Inter-event time between successive earthquakes as a function of W/h^* computed after the cycle converges to a steady state, showing a non-monotonic dependency of inter-event time on LVFZ width.

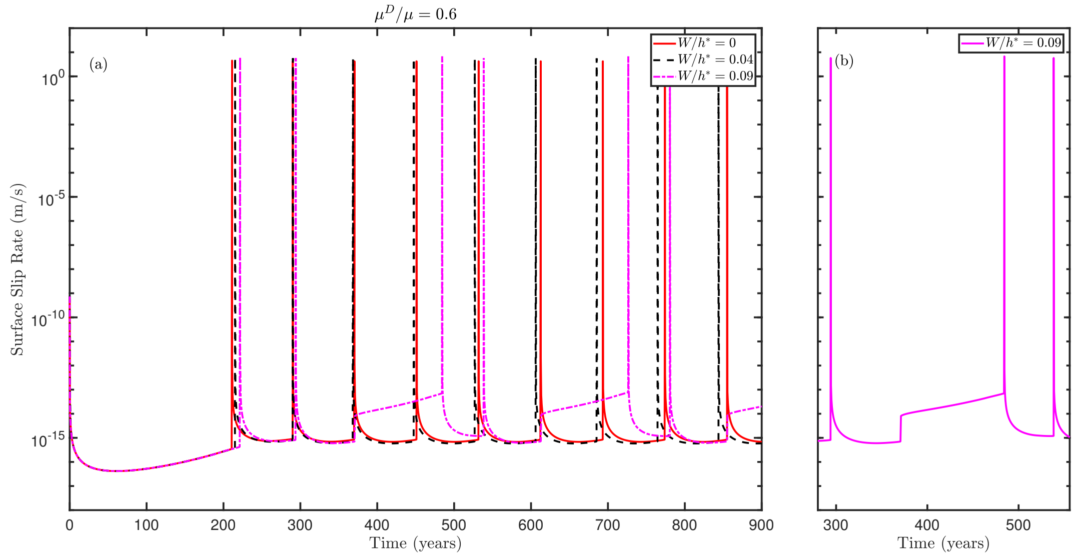

Figure 7: Surface slip rate time history for intermediate rigidity contrast $\mu_D/\mu = 0.6$. (a) Three different cases of varying W/h^*, showing an the impact of the low-velocity fault zone width on the earthquake cycle sequence. (b) A zoomed-in excerpt for the surface slip rate time history for $W/h^* = 0.09$ between 280-550 years showing a kink in the surface slip rate during the subsurface events, corresponding to an increase in the slip rate beyond the background plate loading rate but was not high enough to reach seismic rates.

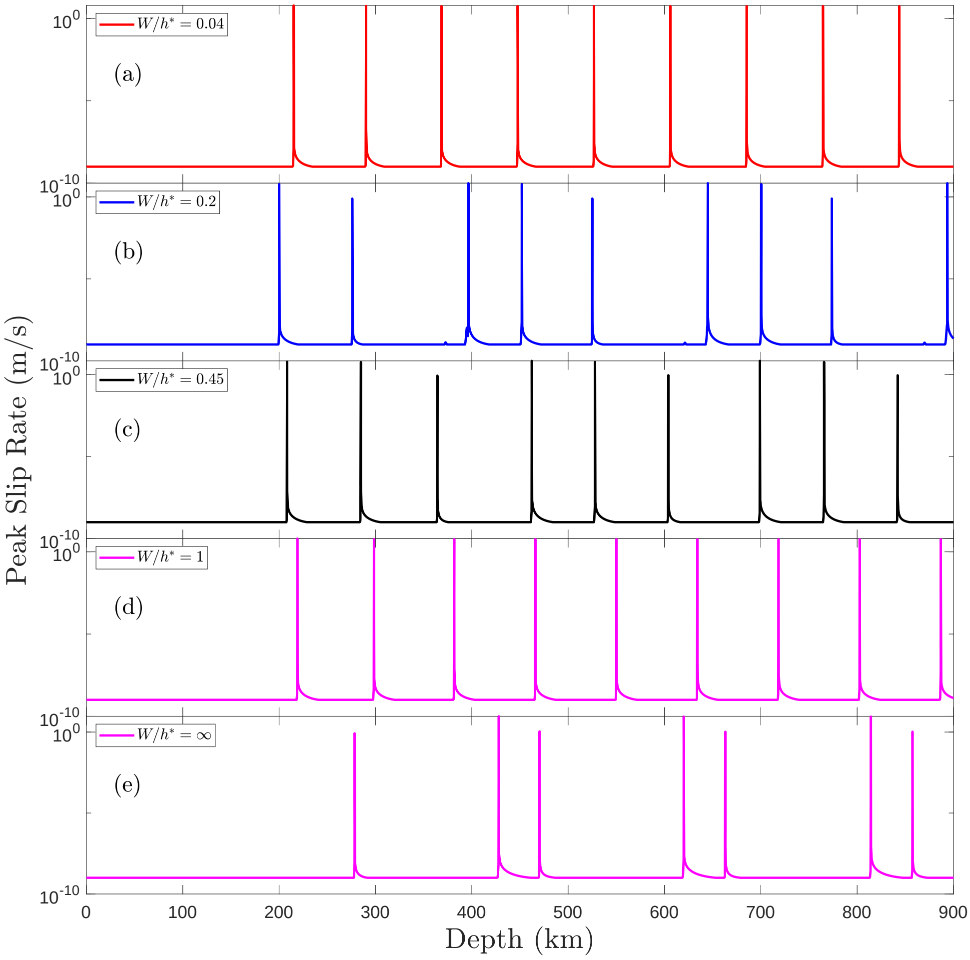

Figure 8: A comparison of the peak slip rate history for various low-velocity fault zone width W and $\mu_D/\mu = 0.6$, illustrating its impact on the earthquake sequence. (a) An earthquake cycle for $W/h^* = 0.04$ showing a periodic sequence of events. (b-c) A complex earthquake sequence emerges that converges to three successive events followed by a delay. (d) An earthquake cycle for $W/h^* = 1$ showing again a periodic sequence of events. (e) A sequence of alternating surface reaching and sub-surface events in a homogeneous bulk structure with $\mu = 19.2$ GPa corresponding to a fully damaged media.

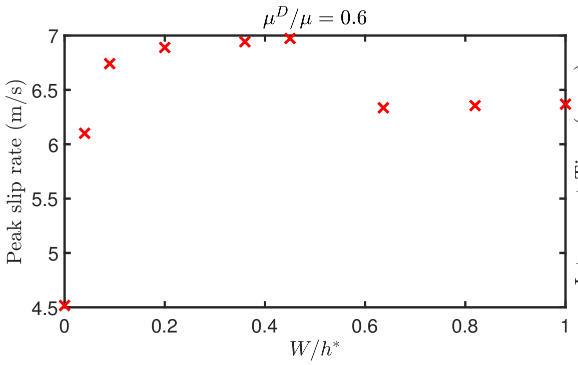

(a)

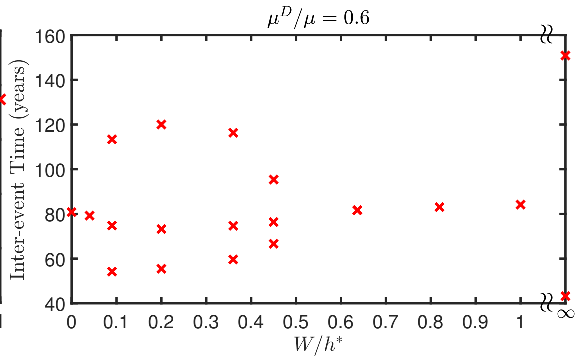

(b)

Figure 9: A comparison of the effect of W/h^* on a low-velocity fault zone with $\mu_D/\mu = 0.6$ with emerging complexities. (a) The maximum peak slip rate as a function of W/h^*. The slip rate amplification is larger in this case compared to $\mu_D/\mu = 0.8$. It is also larger as LVFZ width increase, at least for sequences with both sub-surface and surface reaching events. (b) The inter-event time at a steady state capturing the periodicity of occurrences. Multiple points indicate cluster rather than single-event periodicity, whereas each cluster may consist of two or three seismic events.

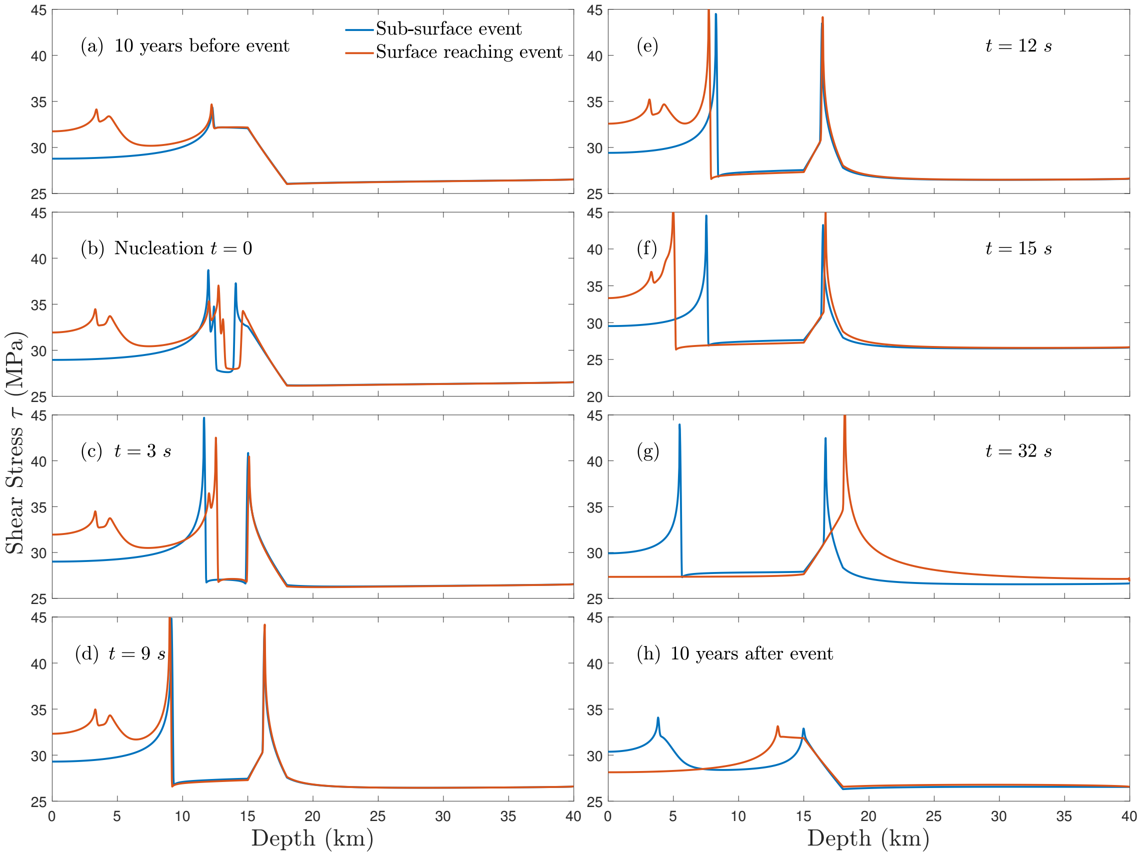

Figure 10: Snapshots of shear stress comparing a surface reaching event (red) and a sub-surface event (blue). (a) 10 years before the event. (b-g) During the event. (h) After the event. The sub-surface events contribute to a residual stress concentration in the vicinity of the rupture arrest. Demonstrated for $W/h^* = 0.09$ and $\mu_D/\mu = 0.6$.

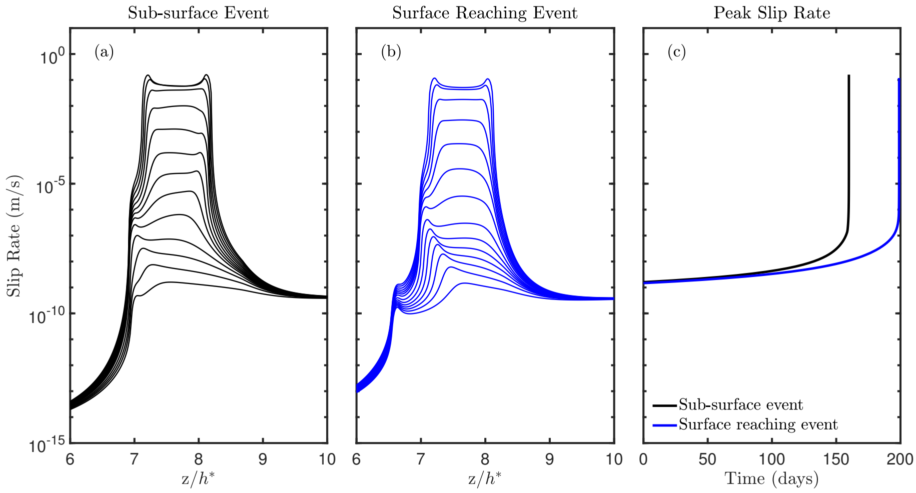

Figure 11: Comparison between the nucleation process in a sub-surface event and a surface reaching event. (a) Snapshots for slip rate as a function of depth ratio z/h^* for a sub-surface event. (b) Snapshots for slip rate for a surface reaching event, suggesting the nucleation process for both sub-surface and surface reaching events are similar. (c) The evolution of the peak slip rate as a function of time for each of the events, suggesting a similar trend for both events. The parameters are identical to those in Figure 10.

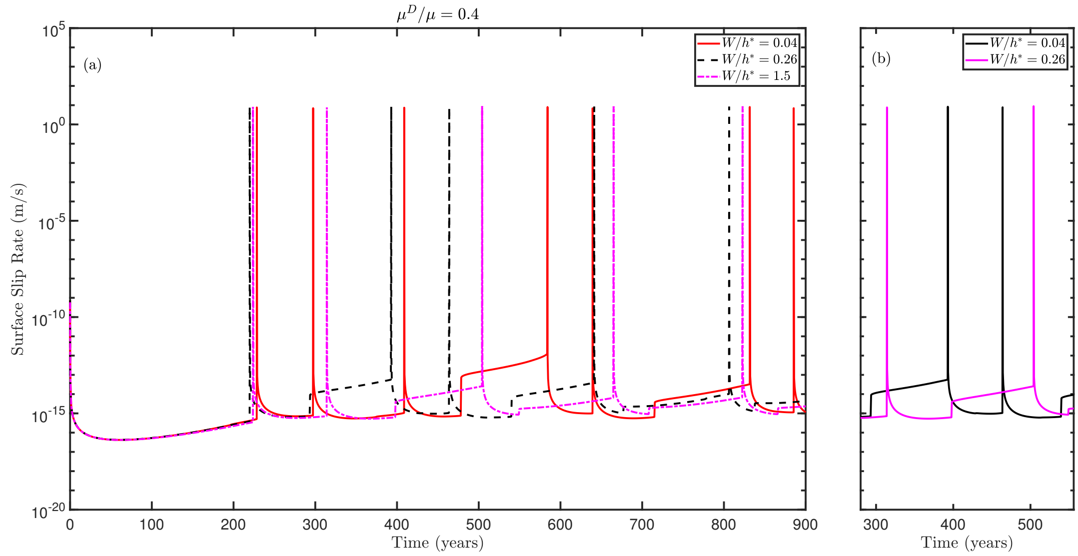

Figure 12: Surface slip rate time history shown for three different cases of varying W/h^* at strong rigidity contrast of $\mu_D/\mu = 0.4$. (a) The low-velocity fault zone width alters the characteristics of the seismic cycle. (b) A zoomed-in excerpt for the surface slip rate time history for $W/h^* = 0.04 - 0.26$ between 280-550 years showing the slight increase in surface slip rate during sub-surface events.

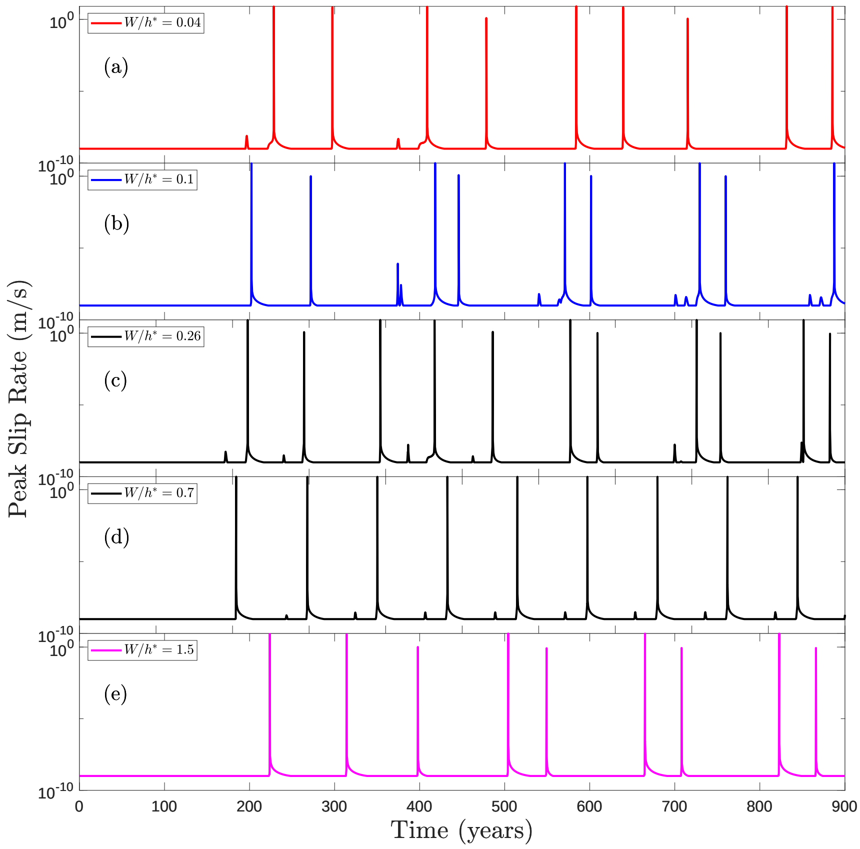

Figure 13: A comparison of the peak slip rate history for various low-velocity fault zone width W and $\mu_D/\mu = 0.4$, illustrating its impact on the earthquake sequence. (a) A complex earthquake sequence emerges that converges to three successive events followed by a delay for $W/h^* = 0.04$, similar to Figure 8c. (b-c) An alternative earthquake sequence emerges that converges to two successive events followed by a delay for $W/h^* = 0.1 - 0.26$. (d) An earthquake cycle for $W/h^* = 0.7$ consisting of a sequence of periodic events. (e) A steady-state behavior of two successive events followed by a delay for $W/h^* = 1.5$.

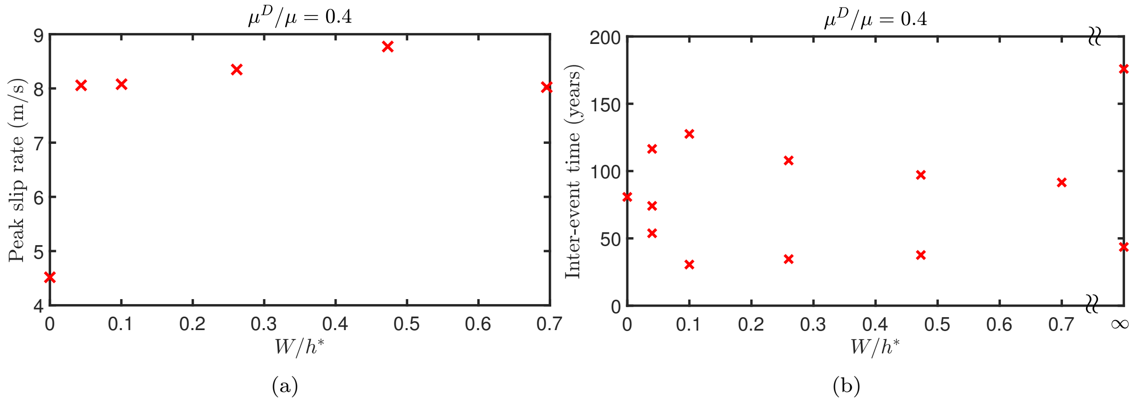

Figure 14: A comparison for the effect of W/h^* on a low-velocity fault zone with $\mu_D/\mu = 0.4$ with emerging complexities. (a) The maximum peak slip rate as a function of W/h^* showing slip rate amplification relative to the homogeneous case. (b) The inter-event time at a steady state capturing the periodicity of occurrences. Multiple points indicate cluster rather than single-event periodicity, whereas each cluster may consist of two or three seismic events.

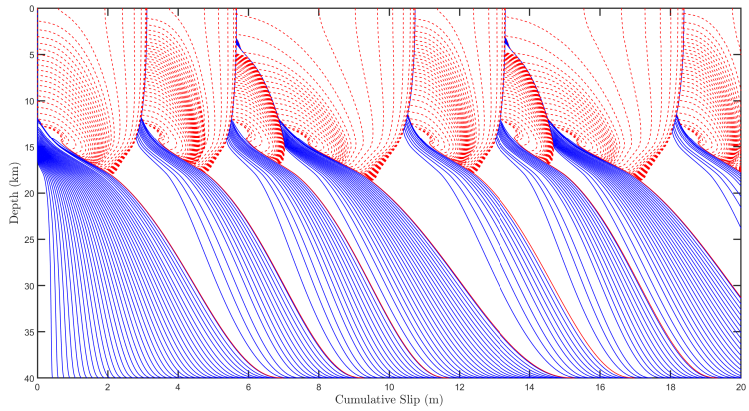

(a)

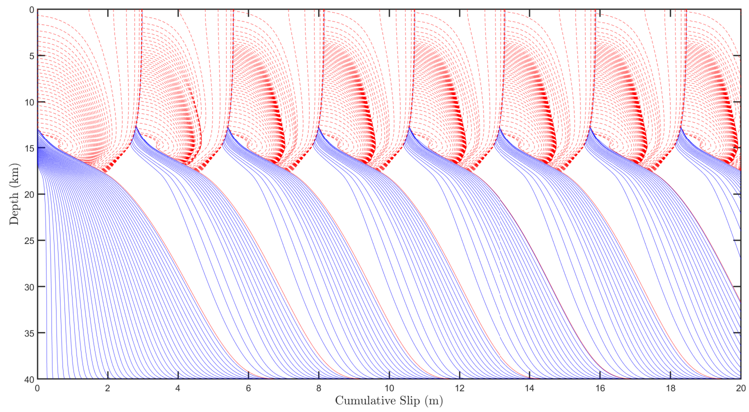

(b)

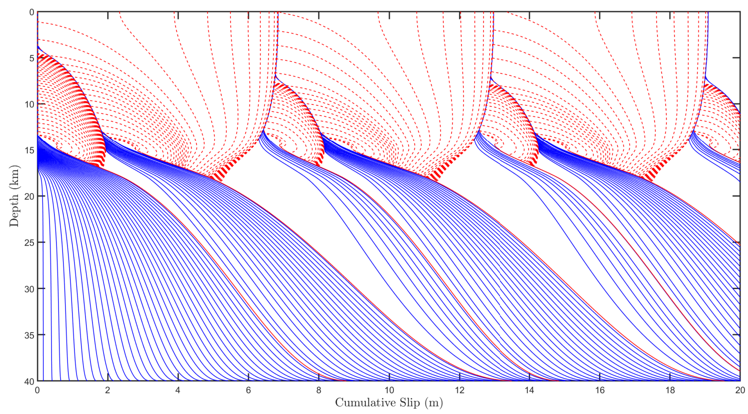

(c)

Figure A1: Snapshots of cumulative slip profiles for $\mu_D/\mu = 0.6$. Solid blue lines plotted at five-year intervals during aesismic slip when peak slip rate is of the order 10^{-3}; red lines plotted at every one second during quasi-dynamic rupture. (a) LVFZ with width $W/h^* = 0.09$. (b) LVFZ with width $W/h^* = 0.65$. (c) LVFZ with width $W/h^* = \infty$.

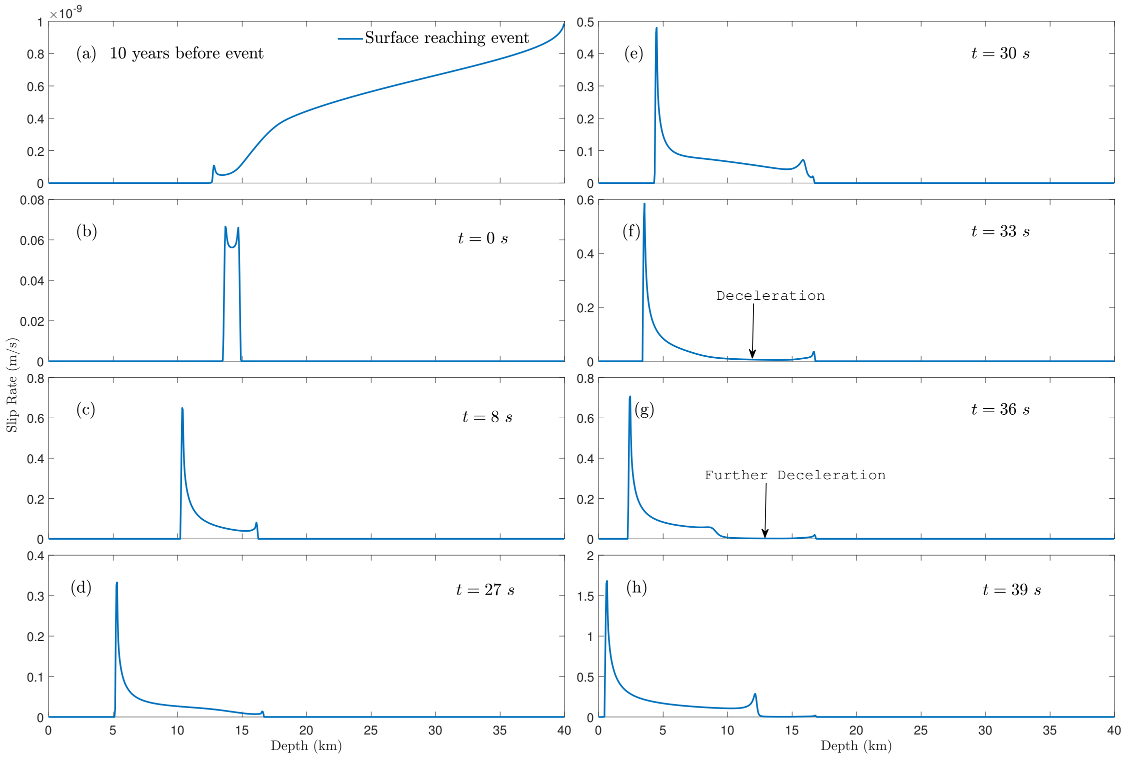

Figure A2: Snapshots of slip rate for $\mu_D/\mu = 0.6$ and $W/h^* = 0.65$. (a) 10 years prior to the event occurrence. (b-e) Quasi-dynamic rupture propagation. (f) At $t = 33\ s$ the rupture decelerates near the VS region. (g) Further deceleration near the VS region. (h) One rupture front propagates to the free surface while another front re-emerges and propagates backward toward the VS region.

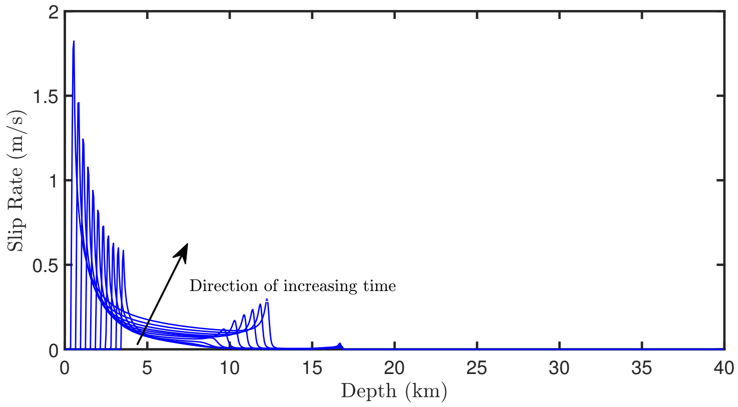

Figure A3: Snapshots of slip rate for $\mu_D/\mu = 0.6$ and $W/h^* = 0.65$ between $t = 33 - 39$ s, showing the rapid back propagating front.